Model dimensionality effects on the amplification of seismic waves

Babak Poursartip[a], Loukas F. Kallivokas[a,b,*]

[a] Department of Civil, Architectural and Environmental Engineering, The University of Texas at Austin, Austin, TX, USA
[b] The Institute for Computational Engineering & Sciences, The University of Texas at Austin, Austin, TX, USA

ARTICLE INFO

ABSTRACT

Despite recent advances in numerical methods and computer architectures that make it ever more practical to obtain computationally the surface response to idealized or realistic seismic events, while fully accounting for three-dimensional effects due to topography or to heterogeneities, reliance on one-dimensional models persists. As discrepancies between computed and recorded responses still remain, in this study we aim at highlighting the effect the model dimensionality choice has on the discrepancies, in the presence of topographic features and/or heterogeneity.

First, we briefly discuss the components of an integrated seismic-motion simulator that deploys best-practice tools for the study of wave amplification in arbitrarily heterogeneous sedimentary basins, while also accounting for topography. Then, we report numerical experiments in two and three dimensions for various prototype topography-endowed and layered domains, and compare the motion amplification/de-amplification patterns against one-dimensional simulations, in order to quantify the effects model dimensionality has on surface motion. We conclude that one-dimensional models greatly underestimate the effects of topography and heterogeneity on the amplification of seismic waves; two-dimensional models fair better, but, in general, they too underestimate the response. It appears that, in the presence of topography and complex stratification, there is no suitable alternative other than three-dimensional models to account for reasonable estimates of motion amplification to guide the design of earthquake-resistant structures.

1. Introduction

The modeling of seismic wave motion within a heterogeneous volume of the earth's upper crust, terminated at an irregular surface (Fig. 1(a)), is often oversimplified by adopting a flat-surface model consisting of horizontal semi-infinite layers and a seismic source that transmits vertically propagating plane waves, as shown in Fig. 1(b). Such simplifications may allow for the use of reduced dimensionality models (1D or 2D), which, however, tend to underestimate motion amplification and fail to adequately capture the motion complexity associated with the physical setting (Fig. 1(a)). While many of the discrepancies reported between observations and computed responses can be attributed to the uncertainties associated with the velocity model (material properties) of a given site, model choices also play a role in the discrepancies. In this article, we highlight the effects model dimensionality has on the motion amplification, in the presence of topographic features or soil heterogeneity.

Numerous documented observations following large earthquakes point to the fact that local site conditions may induce amplification and result in significant motion variability in space. Examples include: Pratt

et al. [1] observed an amplification of up to 16 for the ground motions from the Chi-Chi earthquake in the Seattle basin; Çelebi [2] reported a frequency-dependent amplification of seismic waves due to the surface topography in the 1985 Chile earthquake; Çelebi [3] addressed topographic amplification for a particular range of frequencies; Hartzell et al. [4] and Bouchon and Barker [5] documented several topographic amplifications in California; Assimaki et al. [6,7] observed seismic amplifications in the vicinity of a cliff crest during the 1999 Athens earthquake in Greece and claimed that this amplification can only be predicted by simultaneously accounting for the topographic geometry, stratigraphy, and nonlinearity; Graizer [8] showed that the observed amplification at the Tarzana Hill station from the 1987 Whittier Narrows and the 1994 Northridge earthquakes were due to the combined effects of topography and layering that resulted in trapped energy within a low-velocity layer near the surface; Imperatori and Mai [9] showed via numerical simulation of the Swiss alpine region that topography and heterogeneity excites surface motion, particularly around 1 Hz. Further reviews on observations on seismic amplification can be found in Massa et al. [10], and Buech et al. [11].

Several studies have shown that numerical solutions underestimate

---

* Corresponding author at: Department of Civil, Architectural and Environmental Engineering, USA.
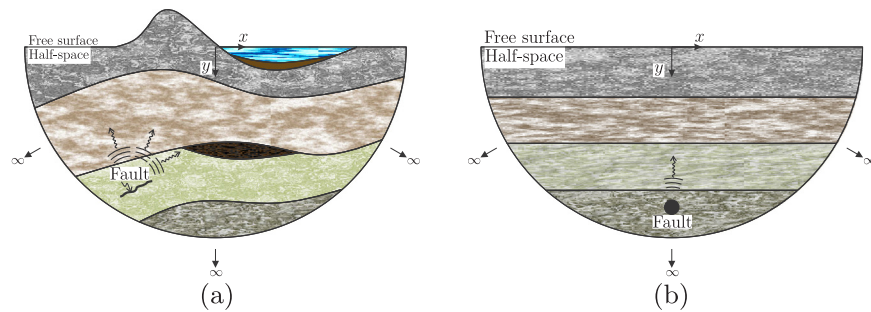 *E-mail addresses:* babakp@utexas.edu (B. Poursartip), loukas@mail.utexas.edu (L.F. Kallivokas).

Fig. 1. Seismic domain of interest: (a) physically-faithful idealization; (b) simplified idealization.

seismic wave amplification. Geli et al. [12] compared experimental observations with theoretical results and concluded that the numerical simulations underestimate the topographic amplifications in most cases, mainly because of the oversimplified assumptions considered in the computational models. Bard [13], based on field evidence and theoretical results, claimed that while there is qualitative agreement between theory and observations, larger amplifications are seen in the field. Semblat et al. [14] focused on the influence of the soil layering complexity on site effects. The authors argued that the geometry of the basin has a strong impact on the amplification of seismic waves and on the lengthening of the shaking duration. Field [15] attributed the spectral amplification variability in a sedimentary valley to the basin-edge-induced waves.

The effects of topography, basin geometry, and stratigraphy have also been studied, more often in isolation of each other, than in combination. For example, one of the earliest attempts at tackling wave scattering due to 3D topographic irregularities is the semi-analytical approach discussed in Sánchez-Sesma [16] for axisymmetric surface features. Dravinski et al. [17] used a boundary element method to study a single-layer sedimentary basin subjected to P, SV, and SH plane waves; Sánchez-Sesma and Luzón [18] analyzed the response of Rayleigh, P- and S- waves in three-dimensional alluvial valleys, while Vai et al. [19] simulated wave propagation in irregularly layered, elastic, two-dimensional media with internal line sources. More recently, Assimaki et al. [6] affirmed the significance of topography by performing a time-domain parametric study on a single slope geometry. They concluded that the frequency content of the excitation, the stratigraphy, and the geometry of the cliff are all important in the amplification of incoming seismic waves. Bouckovalas and Papadimitriou [20] discussed the effects of a step-slope topography on the amplification of vertically propagating SV-waves in the frequency domain; Semblat et al. [14] and Makra et al. [21] studied seismic wave amplification in the Volvi (Greece) site to conclude that the basin's geometry strongly affects motion amplification and motion duration, while Meza-Fajardo et al. [22] obtained amplification factors for 3D alluvial basins compared to 1D models, also in the frequency domain.

Poursartip et al. [23] explored the effects two-dimensional hills and valleys have on the amplification of plane SV- and P-waves via parametric studies in the frequency domain. They classified the influence of a variety of parameters, such as wave frequency, angle of incidence, geometry, and wave types, on the amplification/de-amplification of seismic waves. More recently, Wood and Cox [24] exploited ground shaking generated by the controlled collapse of a coal mine in Utah and reported topography-related effects.

Though several studies targeted the effects of heterogeneity or topography on the amplification of the seismic waves, to date there is limited research studying the differences in the response between the still widely used one-dimensional models and fully three-dimensional models. Notable exceptions include: Makra and Chávez-García [25], who investigated the site effects in the Mygdonian basin in northern Greece using a 3D simulation and compared the results with 1D and 2D models to conclude that, while 2D and 3D models are largely similar,

the 2D model may overestimate the amplification locally. They also claimed that the 1D model underestimates the amplification and motion duration rather remarkably. Riepl et al. [26] compared various 1D and 2D techniques to simulate site effects in basins. Hisada and Yamamoto [27] and Bielak et al. [28] investigated dimensionality effects in a single, elastic layer underlain by an elastic halfspace using harmonic SH waves. Their results indicate that the 1D model exhibits lower amplification and shorter duration than the corresponding 2D and 3D responses. Moreover, they claimed that the destructive interference of waves in 2D and 3D models in certain locations may result in lower amplification compared to the 1D model. Smerzini et al. [29] and Madiai et al. [30] surveyed dimensionality effects in locations in Italy.

Among the various numerical methods that can be used to simulate seismic wave motion, such as finite differences, boundary elements, etc., the spectral element method is possibly better suited, owing to its flexibility in handling heterogeneous domains with complex geometry and its efficiency in parallel implementations (for a review of numerical approaches to seismic simulation see also Semblat [31]). Examples include: Komatitsch and Tromp [32], Komatitsch and Vilotte [33], Peter et al. [34], Poursartip and Kallivokas [35] and Fathi et al. [36]. In order to negotiate the extent of the semi-infinite domain –a key challenge in seismic motion simulations – one can use non-reflecting boundaries as in Kallivokas et al. [37], Bielak et al. [38], Givoli and Neta [39], Hagstrom and Warburton [40], or Perfectly-Matched-Layers –our preferred choice– as in Kucukcoban and Kallivokas [41], and Fathi et al. [36].

The purpose of this study is to investigate the effects model dimensionality may impose on the amplification of seismic waves, by comparing various one-, two-, and three-dimensional prototype models. Towards this end, we developed a spectral element parallel code which is using best-practice tools for wave motion simulation in the time-domain: we deploy Perfectly-Matched-Layers (PML) for truncating the semi-infinite extent of the domain; we introduce the seismic waves within the computational domain via the Domain-Reduction-Method (DRM) [42–45]; we couple the DRM with the PML; and, additionally, we introduce an adaptive time integration scheme that improves the efficiency of the time-domain simulations, particularly for irregular domains where determination of the optimal time-step that leads to a numerically stable solution requires a trial and error approach. Once the numerical tool is verified against known analytical solutions, we use synthetic models endowed with heterogeneity and surface irregularities, to compare the seismic wave amplifications in one-, two-, and three-dimensional domains in order to assess the importance of model dimensionality choice on the surface response.

2. Numerical modeling

To tackle seismic wave simulation within domains exhibiting heterogeneities and/or topographical features, we discuss next the key points of an integrated software toolchain that includes Perfectly-Matched-Layers (PMLs) for limiting the computational domain; unstructured spectral elements for spatial discretization; seismic source
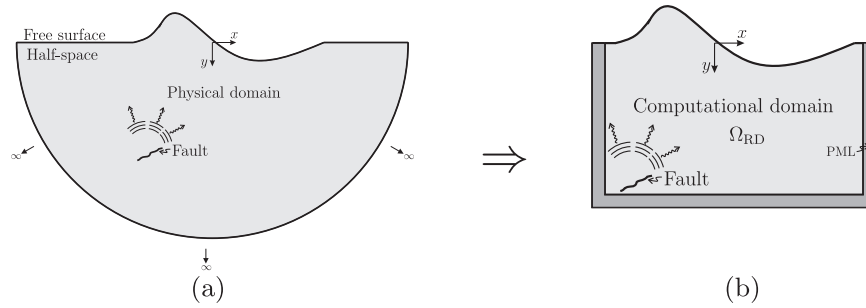
Fig. 2. Physical domain truncation: (a) Semi-infinite domain; (b) Computational domain truncated via PMLs.

modeling using the Domain-Reduction-Method [42–45] that permits placement of seismic sources within the computational domain; and an adaptive time integrator, all cast within a parallel framework that allows for scalable and cost-effective numerical simulations.

2.1. Wave propagation modeling in unbounded domains

Wave motion simulation in unbounded, heterogeneous domains requires negotiation of the semi-infinite extent of the physical domain, which entails the introduction of artificial (non-physical) boundaries surrounding the finite computational domain on the truncation surface, as illustrated in Fig. 2. These boundaries need special treatment in order for the finite domain of interest to mimic the physical behavior of the non-truncated domain, while minimizing spurious reflections that could pollute the solution within the computational domain.

Here, we adopt Perfectly-Matched-Layers (PMLs), among the various methods proposed to treat the truncation boundaries, owing, especially, to their ability to handle heterogeneity. The theoretical aspects of the PML used here are discussed in Kucukcoban and Kallivokas [41] for two-dimensional domains, and in Fathi et al. [36] for the three-dimensional case. According to the mixed-field approach described therein, the governing discrete equation for the wave propagation in a three-dimensional, heterogeneous domain, including the PML, reads [36]:

$$\mathbf{M\ddot{d}} + \mathbf{C\dot{d}} + \mathbf{Kd} + \mathbf{G\bar{d}} = \mathbf{f}, \tag{1a}$$

$$\dot{\bar{\mathbf{d}}} = \mathbf{d}|_{PML}, \tag{1b}$$

where spatial and temporal dependencies are suppressed for brevity, and system matrices, $\mathbf{M}$, $\mathbf{C}$, $\mathbf{K}$, $\mathbf{G}$, and vectors $\mathbf{d}$ and $\mathbf{f}$, are defined as:

$$\mathbf{M} = \begin{bmatrix} \mathbf{M}_{RD} + \mathbf{M}_a^{PML} & \mathbf{0} \\ \mathbf{0} & \mathbf{N}_a^{PML} \end{bmatrix}, \quad \mathbf{C} = \begin{bmatrix} \mathbf{M}_b^{PML} & \mathbf{A}_{eu}^{PML} \\ -\mathbf{A}_{el}^{PML^T} & \mathbf{N}_b^{PML} \end{bmatrix},$$

$$\mathbf{K} = \begin{bmatrix} \mathbf{K}_{RD} + \mathbf{M}_c^{PML} & \mathbf{A}_{pu}^{PML} \\ -\mathbf{A}_{pl}^{PML^T} & \mathbf{N}_c \end{bmatrix}, \quad \mathbf{G} = \begin{bmatrix} \mathbf{M}_d^{PML} & \mathbf{A}_{wu}^{PML} \\ -\mathbf{A}_{wl}^{PML^T} & \mathbf{N}_d^{PML} \end{bmatrix},$$

$$\mathbf{d} = [\mathbf{U} \ \mathbf{\Sigma}]^T, \quad\quad\quad \mathbf{f} = [\mathbf{f}_{RD} \ \mathbf{0}]^T. \tag{2}$$

In these equations, subscript RD refers to the regular (truncated) domain, and $\mathbf{M}_{RD}$, $\mathbf{K}_{RD}$, and $\mathbf{f}_{RD}$, correspond to the standard mass matrix, stiffness matrix, and vector of nodal forces in the interior domain, respectively. $\mathbf{U}$ is the vector of nodal displacements, which is partitioned such that its first entries belong solely to the interior domain, followed by those on the interface boundary between the interior domain and the PML buffer, and, finally, followed by those that are located only within the PML. $\bar{\mathbf{d}}$ is the vector of displacement history, within the PML only, as indicated by (1b), while $\mathbf{\Sigma}$ is the vector of stress components within the PML only. In other words, the solution of (1a) allows the determination of the displacements within the regular domain, and of the displacements and stresses within the PML (thence, the mixed-field designation of the PML treatment). The rest of the submatrices in (2), described in Appendix C for a 3D domain, correspond to the PML buffer zone (see also [36] for submatrix definitions). We note that the PML is not a physical medium (it is not a proper viscoelastic solid), but a mathematical construct, and as such, ascription of mass, stiffness, or damping properties to the PML-designated submatrices is inappropriate. The PML-submatrices collectively account for the motion attenuation within the PML buffer.

2.2. Seismic input modeling

We are interested in accommodating incoming plane seismic waves at various angles of incidence and frequencies, thus, simulating an earthquake originating from the depths of the earth. To this end, rather than simulating the seismic fault directly, we turn to the Domain Reduction Method (DRM), developed by Bielak et al. [42–45], which allows the replacement of the seismic input with equivalent forces deployed over a suitably defined surface in the interior of the computational model. The Domain Reduction Method is a two-step technique. We highlight the steps in the case of topography, but heterogeneities and non-linearities can be similarly treated. During the first step, the free-field solution $\mathbf{u}^0$ due to the seismic source is obtained by subtracting the local geometric irregularities of the region of interest and replacing them with a flat surface domain Ω_0, as depicted in Fig. 3(b). The free-field solution $\mathbf{u}^0$ is obtained within Ω_0 ($\mathbf{u}_i^0$), on the interface
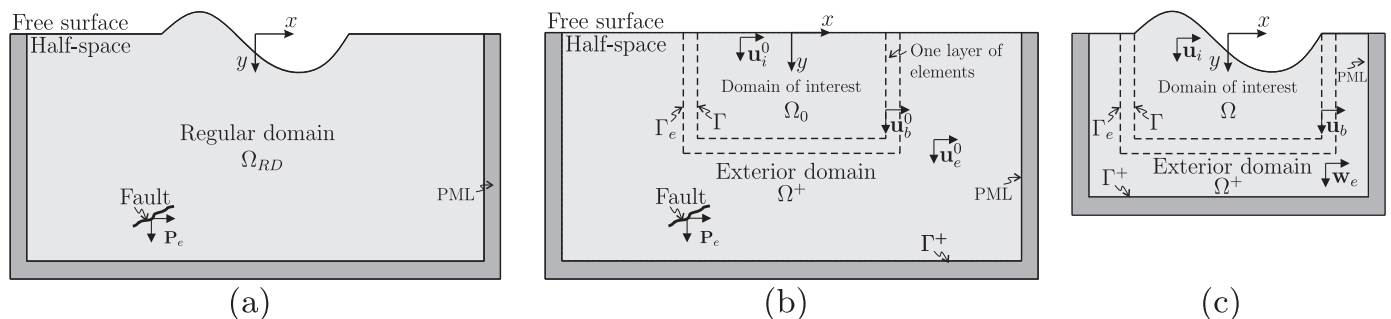

Fig. 3. Steps of the Domain-Reduction-Method: (a) The original model; (b) step I: substituting the domain of interest with a simpler background and obtaining the free-field solution $\mathbf{u}^0$; (c) step II: re-introducing the original domain of interest, the DRM boundary, while eliminating the original seismic source.

between Ω_0 and the exterior domain Ω^+ ($\mathbf{u}_b^0$), and in the exterior domain Ω^+ ($\mathbf{u}_e^0$). In a second step, as shown in Fig. 3(c), the topographic features are re-introduced and the equations of motion are appropriately modified to account for the incoming motion. The latter is accomplished by the introduction of the DRM boundary –a one-element-thick layer– which divides the domain into an interior region of interest Ω, where the unknown is the total motion, and, an exterior region Ω^+ between the DRM and the PML, where the scattered motion becomes the unknown. It is on the DRM boundary that the incoming seismic motion is prescribed (see [43] for details).

We remark that when the free-field solution $\mathbf{u}^0$ of the first step is readily available (e.g., analytically), the method reduces to the second step only. Additionally, since it is not necessary to include the source in the second step, the exterior domain Ω^+ as shown in Fig. 3(c), can be further reduced. In the schematic sequence depicted in Fig. 3, it is tacitly assumed that the physical domain is homogeneous, however, heterogeneities within the domain of interest can be treated similarly, while the exterior domain Ω^+ is also heterogeneous. In the latter case, the free-field solution must be obtained numerically.

To couple the PML with the DRM formulation, (1) must be modified to read:

$$\widetilde{\mathbf{M}}\ddot{\widetilde{\mathbf{d}}} + \widetilde{\mathbf{C}}\dot{\widetilde{\mathbf{d}}} + \widetilde{\mathbf{K}}\widetilde{\mathbf{d}} + \widetilde{\mathbf{G}}\bar{\bar{\widetilde{\mathbf{d}}}} = \widetilde{\mathbf{f}}, \tag{3a}$$

$$\dot{\bar{\bar{\widetilde{\mathbf{d}}}}} = \widetilde{\mathbf{d}}|_{\mathrm{PML}}. \tag{3b}$$

The new system matrices, $\widetilde{\mathbf{M}}$, $\widetilde{\mathbf{C}}$, $\widetilde{\mathbf{K}}$, and $\widetilde{\mathbf{G}}$, and vectors $\widetilde{\mathbf{d}}$ and $\widetilde{\mathbf{f}}$, are defined as:

$$\widetilde{\mathbf{M}} = \begin{bmatrix} \mathbf{M}_{ii}^{\Omega} & \mathbf{M}_{ib}^{\Omega} & \mathbf{0} & \mathbf{0} \\ \mathbf{M}_{bi}^{\Omega} & \mathbf{M}_{bb}^{\Omega} + \mathbf{M}_{bb}^{\Omega^+} & \mathbf{M}_{be}^{\Omega^+} & \mathbf{0} \\ \mathbf{0} & \mathbf{M}_{eb}^{\Omega^+} & \mathbf{M}_{ee}^{\Omega^+} + \mathbf{M}_a^{\mathrm{PML}} & \mathbf{0} \\ \mathbf{0} & \mathbf{0} & \mathbf{0} & \mathbf{N}_a^{\mathrm{PML}} \end{bmatrix}, \quad \widetilde{\mathbf{C}} = \begin{bmatrix} \mathbf{0} & \mathbf{0} & \mathbf{0} & \mathbf{0} \\ \mathbf{0} & \mathbf{0} & \mathbf{0} & \mathbf{0} \\ \mathbf{0} & \mathbf{0} & \mathbf{M}_b^{\mathrm{PML}} & \mathbf{A}_{eu}^{\mathrm{PML}} \\ \mathbf{0} & \mathbf{0} & -\mathbf{A}_{el}^{\mathrm{PML}T} & \mathbf{N}_b^{\mathrm{PML}} \end{bmatrix},$$

$$\widetilde{\mathbf{K}} = \begin{bmatrix} \mathbf{K}_{ii}^{\Omega} & \mathbf{K}_{ib}^{\Omega} & \mathbf{0} & \mathbf{0} \\ \mathbf{K}_{bi}^{\Omega} & \mathbf{K}_{bb}^{\Omega} + \mathbf{K}_{bb}^{\Omega^+} & \mathbf{K}_{be}^{\Omega^+} & \mathbf{0} \\ \mathbf{0} & \mathbf{K}_{eb}^{\Omega^+} & \mathbf{K}_{ee}^{\Omega^+} + \mathbf{M}_c^{\mathrm{PML}} & \mathbf{A}_{pu}^{\mathrm{PML}} \\ \mathbf{0} & \mathbf{0} & -\mathbf{A}_{pl}^{\mathrm{PML}T} & \mathbf{N}_c^{\mathrm{PML}} \end{bmatrix}, \quad \widetilde{\mathbf{G}} = \begin{bmatrix} \mathbf{0} & \mathbf{0} & \mathbf{0} & \mathbf{0} \\ \mathbf{0} & \mathbf{0} & \mathbf{0} & \mathbf{0} \\ \mathbf{0} & \mathbf{0} & \mathbf{M}_d^{\mathrm{PML}} & \mathbf{A}_{wu}^{\mathrm{PML}} \\ \mathbf{0} & \mathbf{0} & -\mathbf{A}_{wl}^{\mathrm{PML}T} & \mathbf{N}_d^{\mathrm{PML}} \end{bmatrix},$$

$$\widetilde{\mathbf{f}} = \begin{bmatrix} \mathbf{0} \\ -\mathbf{M}_{be}^{\Omega^+}\ddot{\mathbf{u}}_e^0 - \mathbf{K}_{be}^{\Omega^+}\mathbf{u}_e^0 \\ \mathbf{M}_{eb}^{\Omega^+}\ddot{\mathbf{u}}_b^0 + \mathbf{K}_{eb}^{\Omega^+}\mathbf{u}_b^0 \\ \mathbf{0} \end{bmatrix}, \quad\quad \widetilde{\mathbf{d}} = [\mathbf{u}_i \;\; \mathbf{u}_b \;\; \mathbf{w}_e \;\; \boldsymbol{\Sigma}]^T. \tag{4}$$

Effectively, $\mathbf{M}_{\mathrm{RD}}$ and $\mathbf{K}_{\mathrm{RD}}$ of (2) have been partitioned to reflect the introduction of the DRM interface; here, $\Omega_{\mathrm{RD}} = \Omega \cup \Omega^+$. The subscripts i, b, and e refer to the nodes within the domain of interest, on the DRM boundary, and in the exterior domain, respectively. The unknown vector $\widetilde{\mathbf{d}}$ comprises four different variables: $\mathbf{u}_i$ and $\mathbf{u}_b$ are the total displacements in the interior domain Ω and on the DRM boundary; $\mathbf{w}_e$, however, are the displacements of the scattered motion in the exterior domain Ω^+ and within the PML buffer zone, and $\boldsymbol{\Sigma}$ are the scattered motion stresses within the PML only, as also indicated in Fig. 3(c). Notice that in the DRM, we decompose the total displacement in the exterior domain of the original model $\mathbf{u}_e$ into the sum of the free-field displacement from the auxiliary model $\mathbf{u}_e^0$ and the scattered field $\mathbf{w}_e$:

$$\mathbf{u}_e = \mathbf{u}_e^0 + \mathbf{w}_e. \tag{5}$$

Per [43], it is this decomposition that allows us to replace the seismic input with equivalent nodal forces in the load vector, as indicated in (4), obtained from the free-field solution recovered during the first step. Accordingly, to introduce the effect of the seismic load, we only need to store the free-field solution in a single layer of elements on the DRM boundary between Γ and Γ_e (Fig. 3(b)).

2.3. Numerical solvers

Implicit transient analysis, whenever possible, is superior to explicit solvers because there is no inherent limit on the size of the time-step, whereas, by contrast, the time-step in an explicit analysis must be less than the CFL limit, in order to have a numerically stable solution. As such, implicit time-steps are often larger than the explicit time-steps. On the other hand, explicit solvers are preferred in parallel implementations due to computational cost considerations. Here, we are interested in reducing the per time-step cost. To this end: we use spectral elements for spatial discretization, we convert the semi-discrete form (3) to first-order in time, and adopt an adaptive time integrator to march in time. The integrator alternates between a fourth-order Runge-Kutta scheme (RK-4) with a fixed time-step, and an adaptive time-step Runge-Kutta-Fehlberg (RKF) scheme. Specifically, the semi-discrete system (3) becomes:

$$\begin{bmatrix} \dot{\boldsymbol{d}}_1 \\ \dot{\boldsymbol{d}}_2 \\ \dot{\boldsymbol{d}}_3 \end{bmatrix} = \begin{bmatrix} \mathbf{0} & \mathbf{I} & \mathbf{0} \\ \mathbf{0} & \mathbf{0} & \mathbf{I} \\ -\widetilde{\mathbf{M}}^{-1}\widetilde{\mathbf{G}} & -\widetilde{\mathbf{M}}^{-1}\widetilde{\mathbf{K}} & -\widetilde{\mathbf{M}}^{-1}\widetilde{\mathbf{C}} \end{bmatrix} \begin{bmatrix} \boldsymbol{d}_1 \\ \boldsymbol{d}_2 \\ \boldsymbol{d}_3 \end{bmatrix} + \begin{bmatrix} \mathbf{0} \\ \mathbf{0} \\ \widetilde{\mathbf{M}}^{-1}\widetilde{\mathbf{f}} \end{bmatrix}, \tag{6}$$

where the new variables $\boldsymbol{d}_1$, $\boldsymbol{d}_2$, and $\boldsymbol{d}_3$ are defined as $\boldsymbol{d}_1 = \bar{\bar{\widetilde{\mathbf{d}}}}$, $\boldsymbol{d}_2 = \widetilde{\mathbf{d}}$, and $\boldsymbol{d}_3 = \dot{\widetilde{\mathbf{d}}}$. The use of spectral elements results in a diagonal mass matrix $\mathbf{M}$, which can be inverted trivially.

Adjusting the appropriate time-step to arrive at a stable solution in a fixed time-step algorithm such as RK4 is challenging in explicit solvers. A necessary condition for stability is that the maximum allowable time-step should be less than the required time for the wave with the shortest wavelength to pass through the smallest grid point spacing (CFL limit). This idea, however, does not ensure a stable solution, and finding the maximum possible time-step still needs a trial and error process, because, according to [46], there is no theoretical guidance on how to choose the right time-step. Komatitsch et al. [46] and Casarotti et al. [47] offer a heuristic rule of 50% of the CFL limit for uniform grids, and only 30% to 40% of the CFL limit for highly non-uniform grids. Fathi et al. [36] also suggested, based on numerical experiments in uniform meshes, to limit the time-step to less than 80% of the CFL limit. Their suggestion is quite reasonable for uniform grids, but, for non-uniform grids, the optimal time-step may be considerably lower than the aforementioned suggestion.

Another possibility is to adaptively modify the time-step size during the temporal integration. This is only possible for one-step methods, where a prior step approximation is required to approximate the solution in the next step. The main difficulty with the adaptivity is to find an efficient a posteriori estimator of the local truncation error. Two options are available [48]: (i) a Runge-Kutta time integration scheme with two different step sizes; and (ii) two Runge-Kutta methods of different order, but with the same time-step sizes and stages. The first option requires that the method solves the system twice, which increases the computational effort. But, the second option estimates the local error with no additional functional evaluations.

In this work, we use the adaptive *Runge-Kutta-Fehlberg* (RKF) to obviate the need for the trial and error process required to find an optimal time-step [48]. We remark that the total computational cost of the RK-4 (fixed time-step) is less than the RKF (adaptive time-step) in each time-step because the number of function evaluations is higher in the latter scheme. The details are provided in Appendix B.

3. Numerical experiments

We study model dimensionality effects on the amplification of waves via synthetic cases in order to quantify the differences between 1D, 2D, and 3D models, and to highlight the importance of considering the three-dimensional simulations in seismic studies. We claim that while the one- and two-dimensional models may offer preliminary estimates, a complete quantitative understanding of strong motion
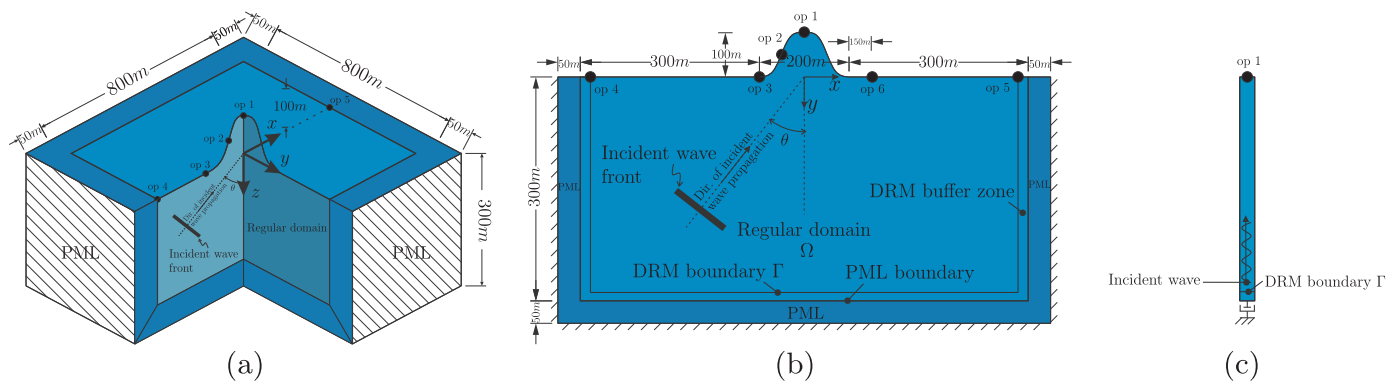
Fig. 4. Schematic figure of the hills with observation points.

requires simultaneous consideration of topography and stratigraphy in a three-dimensional model that includes ideally, the seismic source. Toward this end, we report on model dimensionality effects: (i) in the presence of topography; and (ii) in the presence of heterogeneity.

3.1. Effects of model dimensionality on topographic amplification

We report the effects model dimensionality has on the surface motion in the presence of a hill. The corresponding one-, two-, and three-dimensional models are plotted in Fig. 4. Notice that the two-dimensional model of the hill represents a hill range rather than an isolated hill, and that the one-dimensional model is unable to account for the geometry of the topographic feature.

The geometry of the hill is $y(x) = h\left(1 - \left(\frac{|x|}{b}\right)^2\right)\exp\left(-3\left(\frac{|x|}{b}\right)^2\right)$. The medium is homogeneous with mass density $\rho = 2000$ kg/m^3, Poisson's ratio $\nu = 0.25$, shear wave velocity $c_s = 200$ m/s, and compressional wave velocity $c_p = 350$ m/s. The semi-infinite domain is truncated to an area 800×300 m^2 for the two-dimensional domain and to a volume $800 \times 800 \times 300$ m^3 for the three-dimensional computational domain, surrounded on its sides and bottom by a 50 m-thick PML, as shown in Fig. 4.

The incident excitations are plane P- and SV-waves in the form of a Ricker pulse with a central frequency of 2.0 Hz (Fig. A.27), resulting in a shear wavelength of 100 m, which is equal to the height of the hill. In this case, we discretize the domain using quadratic spectral hexahedral elements with an element (edge) size of 5 m, effectively resulting in approximately 40 points per shear wavelength. The simulations are performed in the time-domain with no material damping. We compare the displacement time histories and their spectra for various models at various observation points (op i, $i = 1, 2, ...,6$) on the surface (Fig. 4). Notice that for the one-dimensional model, there is only one observation point.

Fig. 5 shows the displacement time history at observation point op 1 (hilltop), normalized with respect to the amplitude of the incident wave u_i, due to a vertically propagating P-wave. The horizontal component of the displacement vanishes, owing to the symmetry of the model and of the seismic load. The largest amplification, 4.78, results from the three-dimensional model, and is 2.4 times larger than the amplification predicted by the one-dimensional model. The amplification of the two-dimensional model is 3.11, roughly 1.56 times greater than that of the one-dimensional model, and 1.53 times smaller than that of the three-dimensional model. The larger amplification in the three-dimensional model is mostly due to wave focusing at the hilltop. We note that, in reality, a large amplification at the hilltop or at other sharp feature termination points, such as the edge of a cliff, is likely but will be highly localized and, as we will see later, such large amplifications are not expected at other points on the surface.

We also remark that the total motion duration (until near silence) has almost doubled for the two- and three-dimensional models compared to the one-dimensional simulation (1 s versus 2 s), due to the trapping of the waves within the topographic feature.

The displacement time histories in all three models have similar frequency content, as depicted in Fig. 5; however, the three-dimensional model shows the largest amplitude: while for the central frequency of the wave (2 Hz), the one- and two-dimensional models barely reach 0.37 and 0.65, respectively, the amplitude of the three-dimensional model is 1.0. Notice also that, at the hilltop, all frequencies have been uniformly amplified.

If we repeat the same experiment with a vertically-incident SV wave (Fig. 6), the amplification for the three-dimensional model increases dramatically to 8.78. The maximum amplification of the one-dimensional model is again capped at 2, while the two-dimensional model results in an amplification of 2.96; clearly, the one- and two-dimensional models greatly underestimate the amplification. The frequency spectrum for the three-dimensional model shows greater amplification for all frequencies when compared to the P-wave incidence (Fig. 6(b)).

The displacement time history for observation point 2, located at the middle of the hillside, 50 m away from the hilltop, is shown in Fig. 7. By contrast to the displacement waveform at the hilltop, the waveform at mid-slope shows multiple peaks for both the two- and three-dimensional models, owing to the complex wave interference that is more pronounced at mid-slope than at the hilltop. Even though the maximum displacement in each component is not remarkably greater than that of the one-dimensional model, the combination of the two components shows a relatively stronger motion than the one-dimensional case. The total ground motion duration has increased to more than three seconds, which is more than three times the duration of motion in the one-dimensional model and 50% longer than the motion duration at the hilltop.

The Fourier spectrum of the time history (Fig. 7) reveals more information about the effects of topography: by contrast to the one-dimensional model, certain frequencies exhibit greater amplification than what we observed at the hilltop, while at other frequencies the motion is de-amplified.

Fig. 8 shows the displacement time history at observation point 3, located at the foot of the hill. We can distinguish two separate motions in the time history of the two- and three-dimensional models: the first one, whose waveform resembles the incident wave, is the reflection of the incident wave from the flat surface, and the second part captures waves scattered by the topography. In that second wave-packet of the time history, the two-dimensional model shows a larger amplitude than the three-dimensional model because the two-dimensional model represents a hill range, thus, trapping more energy within the range, than that trapped within the isolated hill. The frequency spectra of the responses show peaks at frequencies that are characteristic of the topographic feature, however, overall, the content is still dominated by the input motion spectrum.

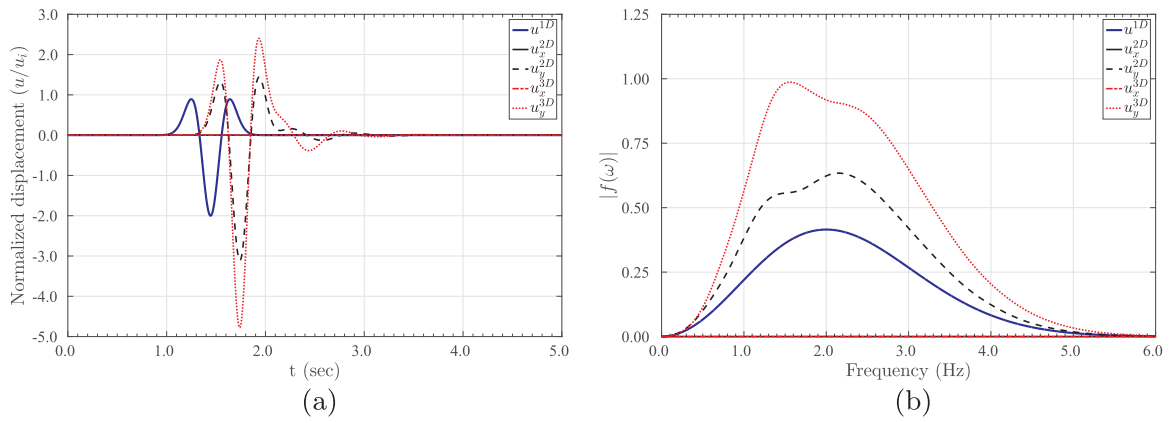The displacement time history for observation point 4, located at

Fig. 5. Comparison of (a) displacement time histories and (b) their frequency spectra at *observation point 1* (hilltop) due to a vertically propagating P-wave for the one-, two-, and three-dimensional hill models.
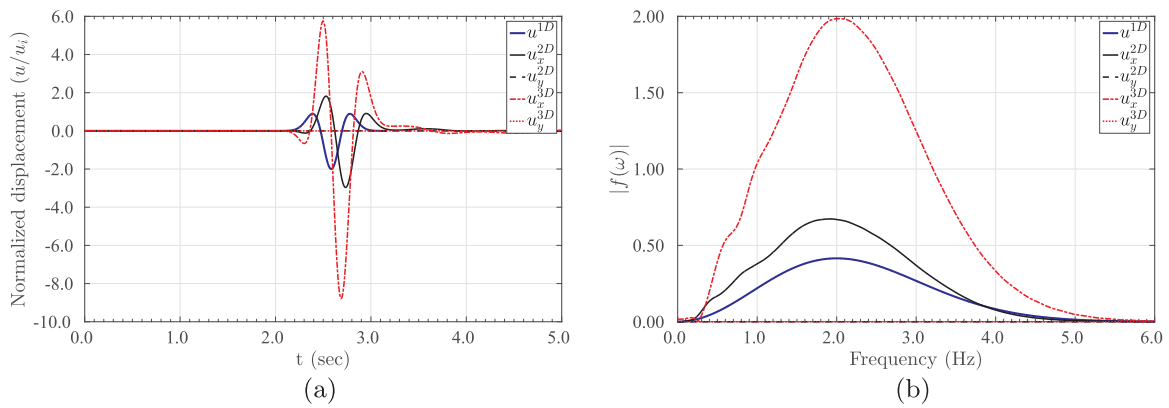

Fig. 6. Comparison of (a) displacement time histories and (b) their frequency spectra at *observation point 1* due to a vertically propagating SV-wave for the one-, two-, and three-dimensional hill models.
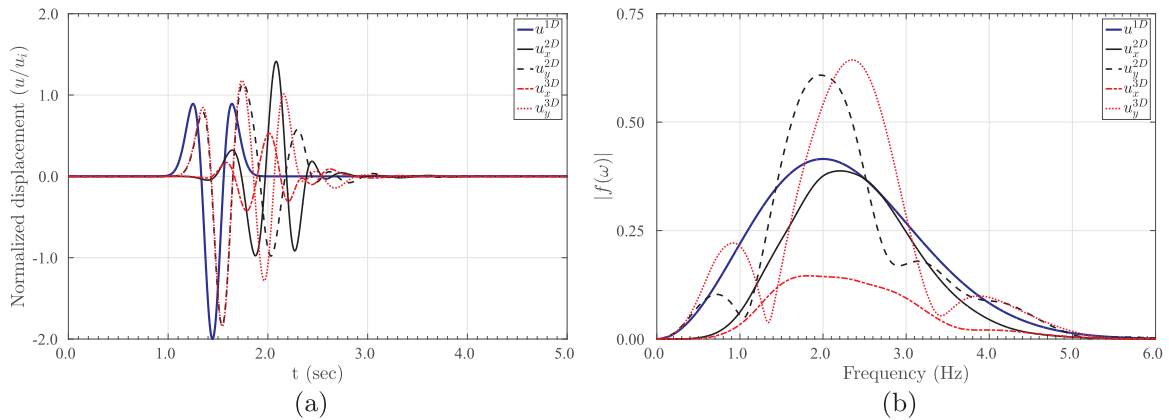

Fig. 7. Comparison of (a) displacement time histories and (b) their frequency spectra at *observation point 2* due to a vertically propagating P-wave for the one-, two-, and three-dimensional hill models.

the farthest point from the feature, is shown in Fig. 9. We can clearly observe the incident wave during the first part of the waveform, followed by the reflections from the topography, that reach point 4 after some delay. Notice that not only the displacements for the two- and three-dimensional models are identical in the first part, but they are also identical to the one-dimensional simulation. That implies that if the main shock is not polluted by the reflected waves from the topography, the displacement time histories on the flat surface for all models are identical, as also predicted from closed-form solutions. The rest of the motion on the flat surface followed by the main shock is the result of

wave reflections, mode conversions in the hill, and, mostly, due to Rayleigh waves, which are not accounted for in a one-dimensional simulation. Even though the amplitude of the reflected waves is not significant in comparison to the main shock, the total shaking duration is increased. Moreover, due to the symmetry of the load and the model, the vertical displacement of the main shock is zero, but the vertical component of the reflected waveform does not vanish and the motion amplitude is greater for the two-dimensional model compared to the three-dimensional model, because, the two-dimensional model resembles a hill range which produces wave reflections from the entire
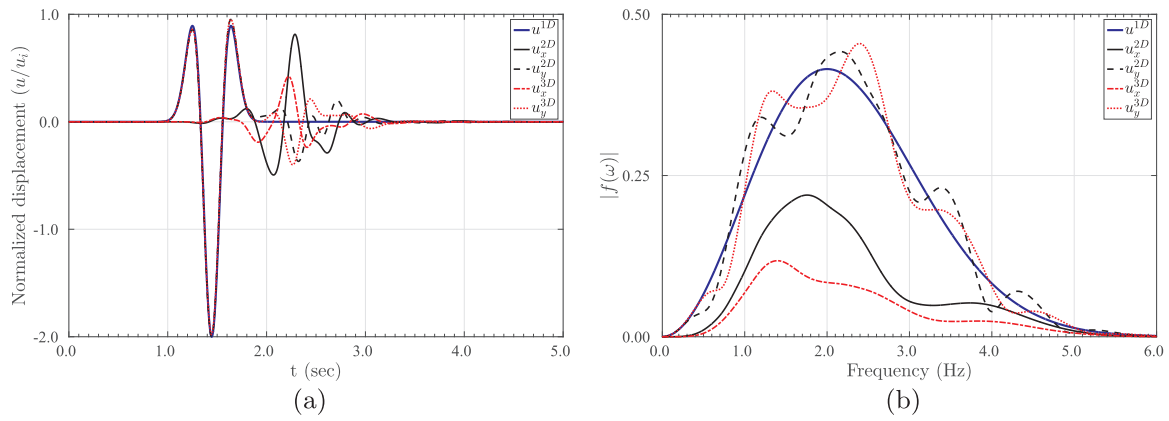
Fig. 8. Comparison of (a) displacement time histories and (b) their frequency spectra at *observation point 3* due to a vertically propagating P-wave for the one-, two-, and three-dimensional hill models.
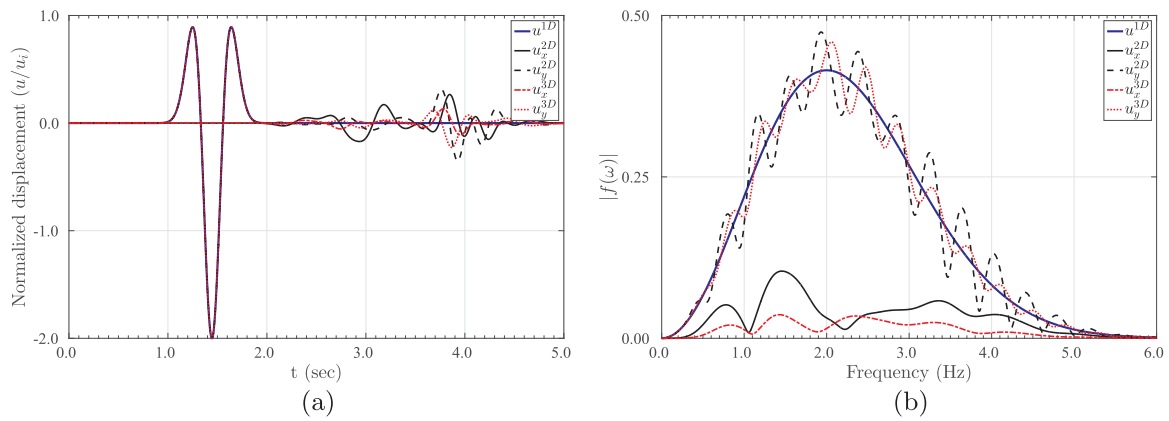

Fig. 9. Comparison of (a) the time histories of displacement and (b) the frequency spectra at the *observation point 4* due to a vertically propagating P-wave for two- and three-dimensional hills.

range, while in the three-dimensional simulation, there is reflection only from the isolated hill. We also remark that the total duration of the incident wave is only 1.2 seconds, which does not allow sufficient time for any interactions –constructive or destructive– between the incident and the scattered waves generated by the topography. In a real earthquake event, with a long duration, the interference of the incident and reflected waves would result in amplification/de-amplification within the hill as well as on the flat surface away from the hill. To study this particular case, we subject the two-dimensional model to five consecutive and amplitude-alternating Ricker pulses. The displacement time history at observation point 6 is plotted in Fig. 10(a), which shows that the displacement on the flat surface amplifies to 2.38 – a 19% increase over the maximum displacement of the single Ricker pulse case. Similarly, amplification occurs at multiple locations away from the hill (Fig. 10(b)).

In conclusion, the presence of topography not only affects the total duration of the motion on the flat surface, but also results in significant amplification. As a result, the region around the topographic feature is also prone to experiencing significant motion amplification, especially if the motion duration is long enough.

Figs. 11 and 12 display the contours of total displacement in the two- and three-dimensional simulations for a vertically propagating SV-wave, respectively. The first snapshot shows the propagation of the incident wave just before it impinges on the surface. The second snapshot shows the displacement right after the incident wave has hit the surface. Then, the incident wave enters the hill and reflects multiple times off of the hillsides. Notice that Rayleigh waves are generated in the domain at the foot of the hill. The third snapshot shows the moment

the maximum displacement is realized, when the generated Rayleigh waves from the two sides of the hill converge to the hilltop. The last snapshot displays the displacement contour right before the main reflected wave-packet leaves the domain. Notice the wave that has been trapped within the hill due to multiple reflections from the hillsides. The Rayleigh waves are also responsible for motion on the flat surface even after the incident wave has left the domain. We remark that the PML buffer zone is clearly visible on the sides and bottom of the models, and, as it can be seen, there are no discernible reflections from the truncation boundaries.

In another experiment, we transmit an oblique SV-wave at an incidence angle $\theta_s = 15°$. Fig. 13 shows the displacement time history at observation point 1. The horizontal displacement in the three-dimensional model is greater than that of the two-dimensional model, 7.24 vs. 1.93, respectively, while the vertical displacements are almost the same, 1.92 vs 1.96. Even though the maximum displacements for the obliquely incident wave are smaller in comparison to the vertically propagating wave, they are still greater than those corresponding to the one-dimensional model. The frequency spectra of the signals indicate that the largest amplification occurs at frequencies that are less than the excitation's central frequency. Fig. 14 shows the displacement time history at observation points 4 and 5, on the two sides of the hill for the obliquely incident wave. The first part of the time histories, i.e., the reflection of the incident from the flat surface, is identical. However, the amplitude of the reflected waves at observation point 4, on the left side of the hill where the plane wave hits first, is less than at point 5, 0.2 versus 0.4, respectively.
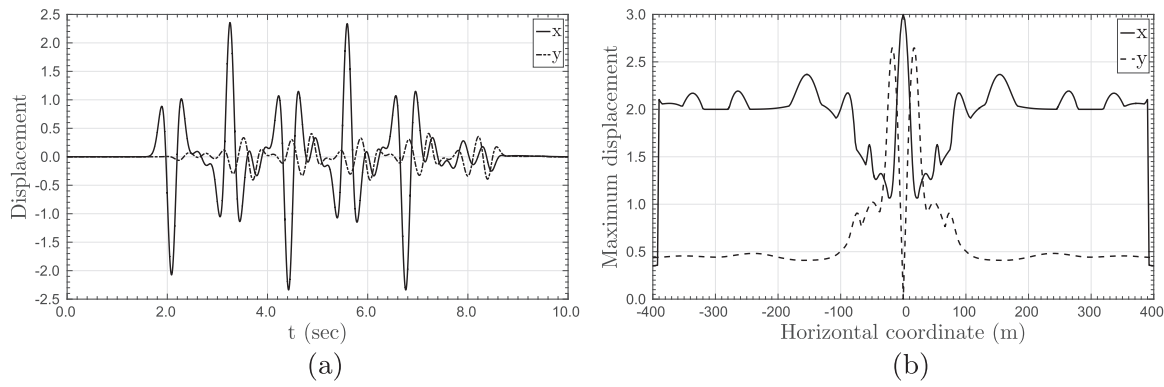
Fig. 10. (a) Displacement time history at observation point 6 for a longer duration incident wave, and (b) maximum surface displacement due to a vertically propagating SV-wave.
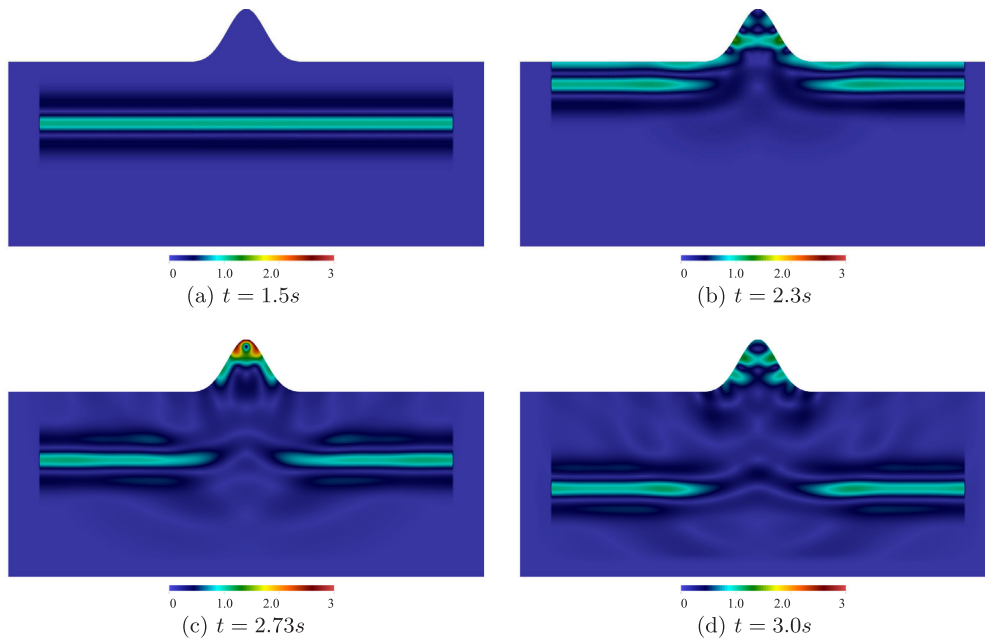

(a) $t = 1.5s$

(b) $t = 2.3s$

(c) $t = 2.73s$

(d) $t = 3.0s$

Fig. 11. Contours of displacement due to a vertically propagating SV wave in the two-dimensional model.

3.2. Effects of model dimensionality on the response of heterogeneous domains

A one-dimensional seismic model is seldom a good approximation for a soil domain: it is only under very restrictive assumptions (e.g., horizontal layering) that such a model would lead to reasonable motion estimates. Observations from past earthquakes show that such simplified models might lead to poor predictions, especially in the case of sedimentary valleys. For example, King and Tucker [49] showed via experiments that a seismic amplification of 10 is possible within the sedimentary valleys, while the surface amplification depends highly on the distance from the edge of the valley, to the extent that, for example, the ground motion at the valley edges may differ from the motion at mid-valley, by as much as a factor of 5, even though the two sites may be separated from each other by as little as 100 m. This behavior cannot be predicted using one-dimensional models.

The goal of this section is to use one-, two-, and three-dimensional models of two synthetic, sedimentary valleys to highlight the dimensionality effects on seismic motion amplification.

3.2.1. Example 1: Homogeneous valley: 1D vs. 2D

Let us consider a two-dimensional, homogeneous, semi-circular, sediment-filled valley, with a radius of 100 m, as shown in Fig. 15. The valley is embedded within a stiffer host. The semi-infinite domain is truncated to an area 800×300 m², surrounded on its sides and bottom by a 25 m-thick PML. The mass density of the host is $\rho = 2000$ kg/m³, the shear wave velocity is $c_s = 300$ m/s, and the compressional wave velocity is $c_p = 489.9$ m/s. We define the soft material within the valley such that the shear and compressional wave velocities are $c_s = 150$ m/s and $c_p = 280.6$ m/s, respectively, with mass density $\rho = 1500$ kg/m³. The medium is linear elastic with no material damping. The equivalent one-dimensional models for the two soil column beneath observation points 1 and 2 (Fig. 15(a)) are plotted in Figs. 15(b) and 15(c).

The PML absorbing layer and the soil surrounding the valley are discretized by quadratic elements with an element size of 2.5 m, resulting in a ten-element-thick PML. The soft sedimentary valley is discretized with elements of size 1.25 m. The excitation is an incident P-wave in the form of a Ricker pulse with a central frequency of $f_r = 3.0$ Hz. Thus, the resulting mesh has about 40 points per shear

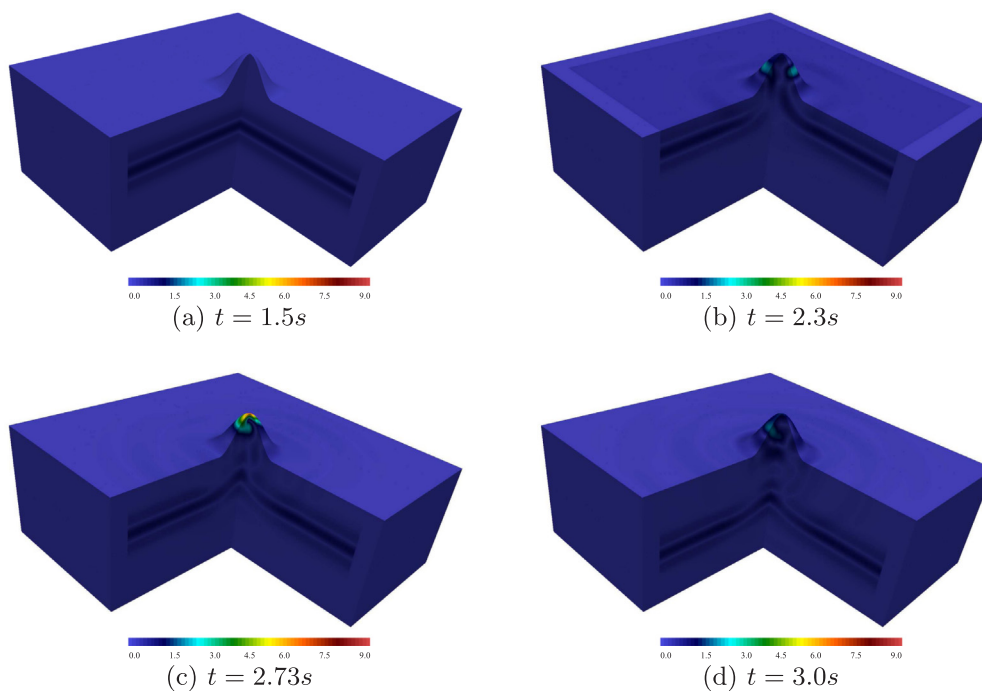(a) $t = 1.5s$

(b) $t = 2.3s$

(c) $t = 2.73s$

(d) $t = 3.0s$

Fig. 12. Displacement contours due to a vertically propagating SV wave in the three-dimensional model.
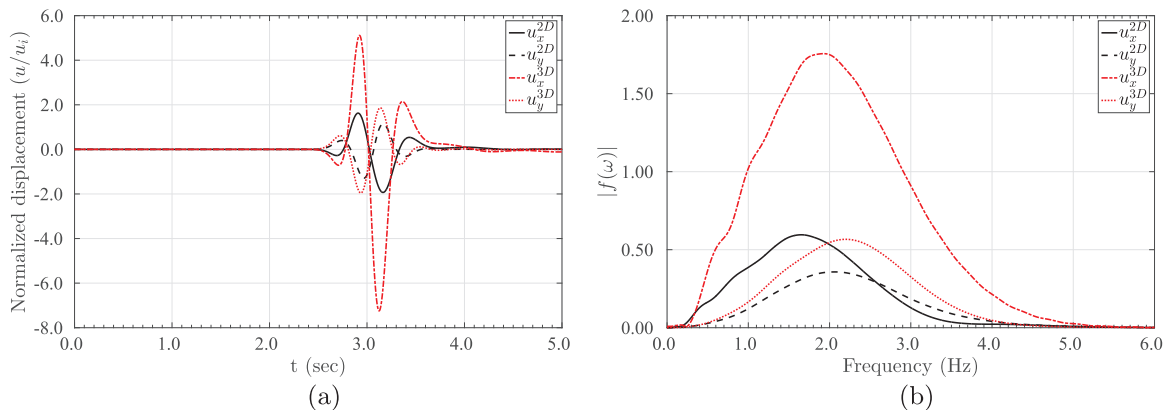

(a)

(b)

Fig. 13. Comparison of (a) displacement time histories of displacement and (b) their frequency spectra at *observation point 1* due to the SV incidence at $\theta_s = 15°$ for the two- and three-dimensional hill models.
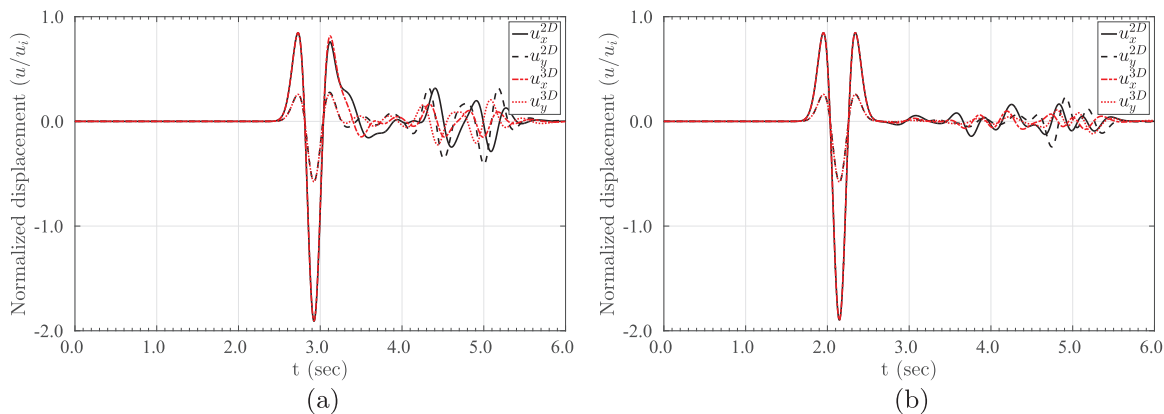

(a)

(b)

Fig. 14. Comparison of displacement time histories of displacements at (a) *observation point 4*, and (b) *observation point 5* due to SV incidence at $\theta_s = 15°$ for the two- and three-dimensional hill models.
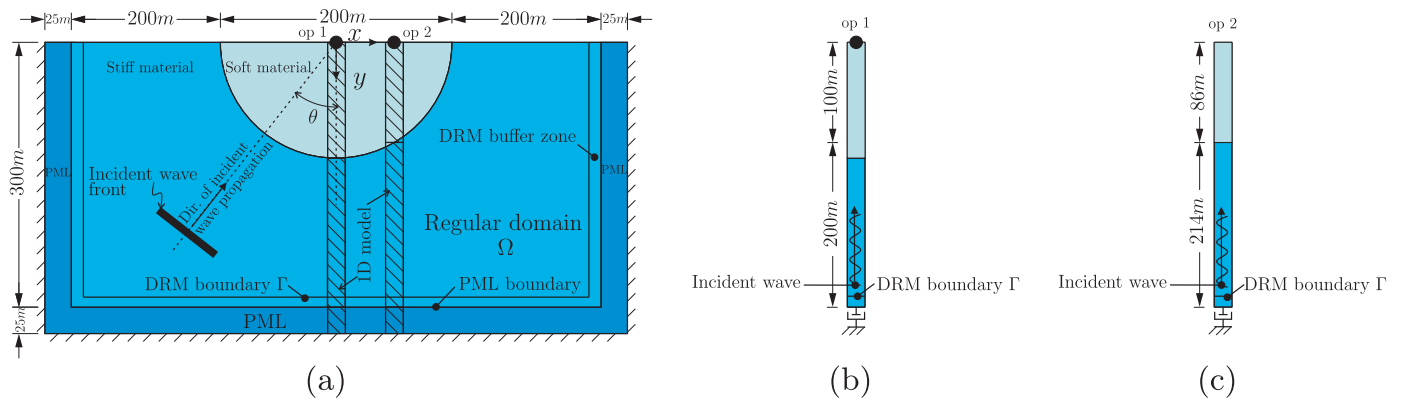
Fig. 15. The computational domain for example 1: (a) the two-dimensional, sediment-filled valley, (b) the equivalent one-dimensional model at observation point 1, and (c) the equivalent one-dimensional model at observation point 2.
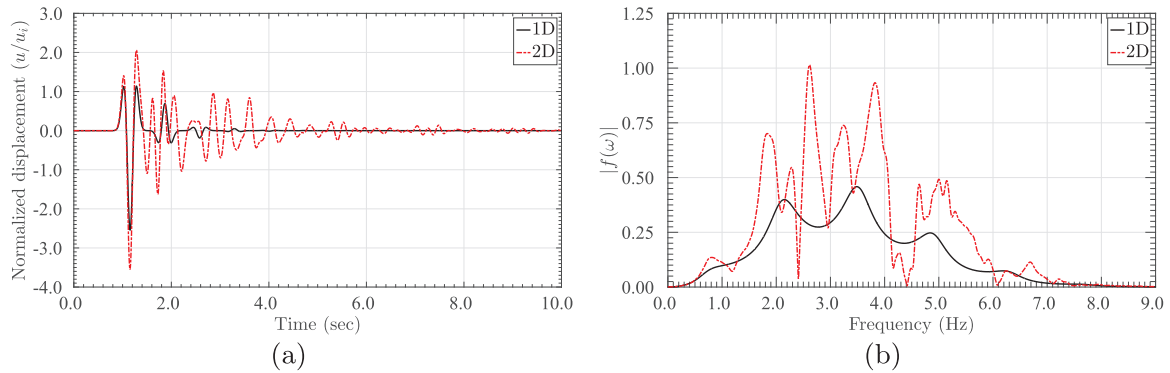

Fig. 16. Comparison between (a) displacement time histories, and (b) their frequency spectra of the one- and two-dimensional models at observation point 1.
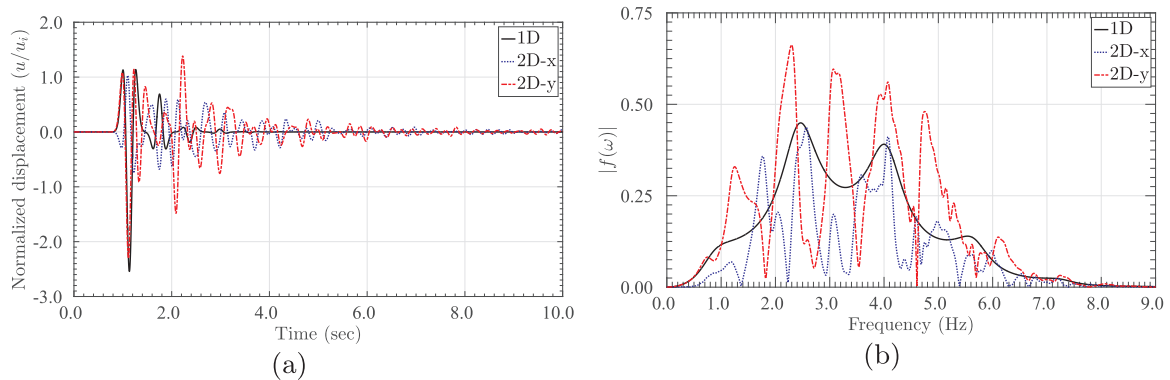

Fig. 17. Comparison between (a) displacement time histories, and (b) their frequency spectra of the one- and two-dimensional models at observation point 2.

wavelength, where the latter corresponds to the central frequency of the Ricker pulse. For the highest frequency content of the Ricker pulse, the points reduce to about 13 per shear wavelength.

The vertical displacement time histories, normalized with respect to the amplitude of the incident wave, and their Fourier spectra at observation point 1 are shown in Fig. 16 along with the equivalent one-dimensional model results. Notice that, owing to the symmetry of the domain and of the load, the horizontal displacement in the two-dimensional simulation vanishes at this point. The maximum displacements are 2.54 versus 3.54, for the one- and two-dimensional simulations, respectively. In other words, the two-dimensional simulation results in 40% larger displacement at that particular point. Additionally, while the motion in the one-dimensional simulation consists of a few isolated pulses, the two-dimensional model exhibits a longer lasting motion with large amplitudes. In other words, the one-dimensional simulation substantially underestimates the surface motion.

Let us turn our attention to the frequency spectra of the displacements at this observation point, depicted in Fig. 16(b). The first 3 theoretical amplification frequencies[1] for the 1D model are 0.702 Hz, 2.105 Hz, and 3.508 Hz; they are clearly recovered in the 1D spectrum of Fig. 16(b). However, notice that the two-dimensional amplification frequencies are different from those of the one-dimensional model. The largest amplification in the one-dimensional model is only 0.46 (at 3.508 Hz), while for the two-dimensional model, the maximum amplification is 1.015 at 2.7 Hz. The two spectra are fundamentally different, both in terms of the amplification frequencies and in terms of the associated amplitudes.

---

[1] It can be shown that the amplification frequencies of the one-dimensional soft layer over half-space are the same as the natural frequencies of the layer on a fixed base, given as $\frac{2n-1}{4H}c_p$ for $n = 1, 2, \ldots$ and H the height of the layer.
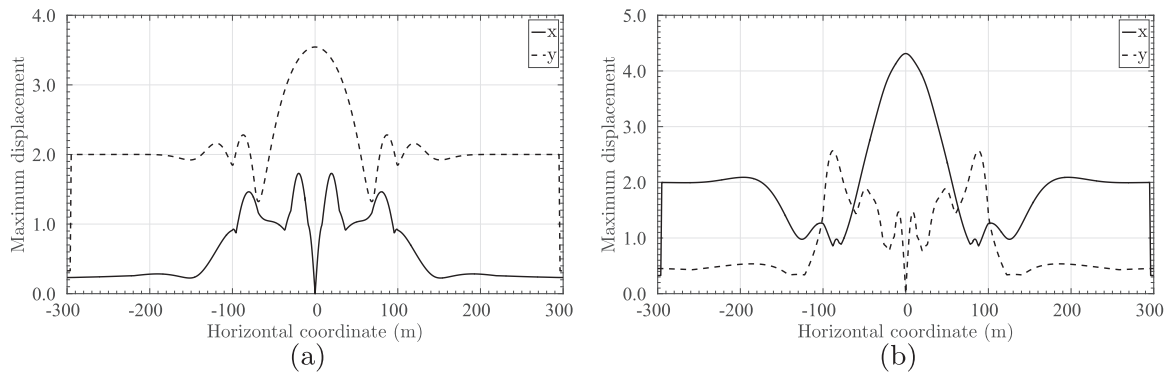
Fig. 18. Maximum surface displacement in the two-dimensional, homogeneous, sedimentary valley due to a vertically propagating (a) P wave, and (b) SV wave.
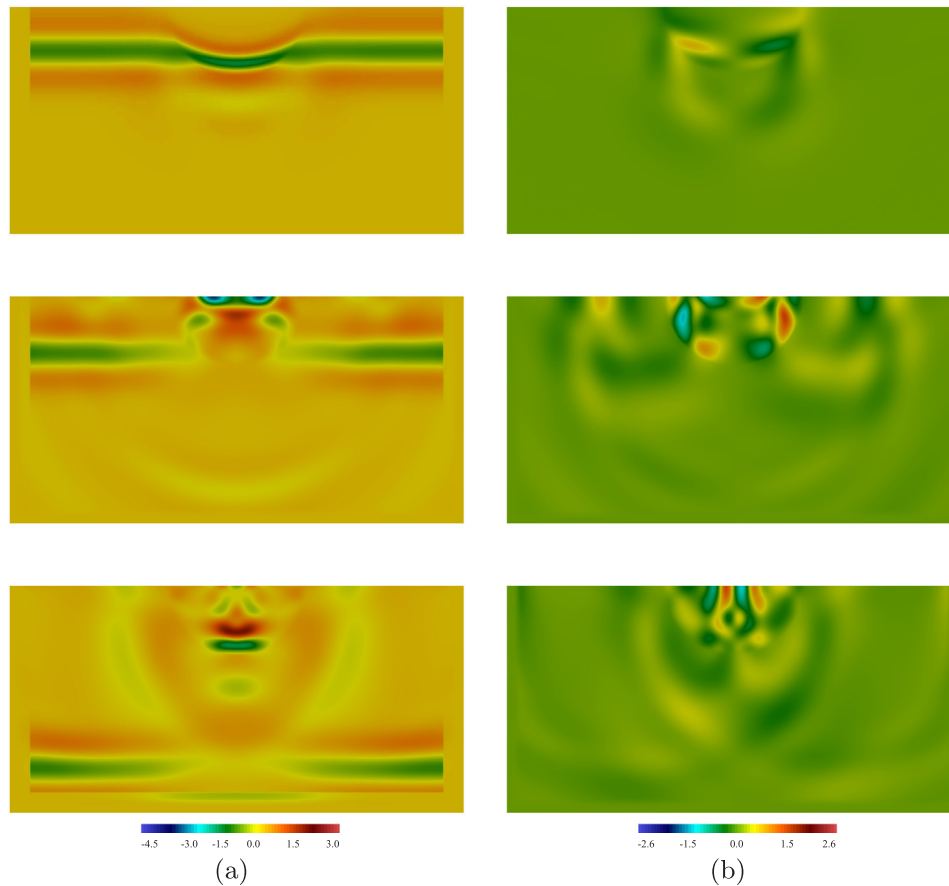

Fig. 19. Contour of displacements in the *x* and *y* directions due to a vertically propagating SV-wave: (a) displacement in the X direction, and (b) displacement in the Y direction.

The time histories of the horizontal and vertical displacements for observation point 2, located 50 m away from the midpoint of the valley, are shown in Fig. 17(a). At this point (op2), the maximum displacement of the two-dimensional model is smaller in comparison to the first observation point (op1), while the maximum displacement of the one-dimensional simulation has remained the same. The maxima are comparable, 2.30 versus 2.54 for the one- and two-dimensional models, respectively. The main difference here is the presence of horizontal motion in the two-dimensional model, which cannot be predicted by the one-dimensional model. The horizontal displacement is as large as 1.85, and if it is combined with the vertical displacement, the total displacement would be greater than the one predicted by the one-dimensional model. The frequency spectra of the displacements from the two simulations, shown in Fig. 17(c), differ both in amplitude and in the dominant frequencies.

We note that the maximum displacement in the one-dimensional simulation is constant, regardless of the depth of the soft layer and the frequency of the signal, yet, the amplification frequencies are different for each depth. By contrast, the maximum surface displacement for the two-dimensional model, depicted in Fig. 18(a), varies by surface location, owing to the wave interactions within the soft sediment (the valley extends between − 100 m and 100 m). The maximum horizontal displacement is 3.54, occurs at the midpoint of the sedimentary valley, while the maximum vertical displacement is 1.73 and occurs closer to the edge of the valley. If we consider the total displacement on the surface, the one-dimensional model underestimates the amplification at the middle of the valley in comparison to the two-dimensional model, while it overestimates the amplification closer to the edge of the valley.
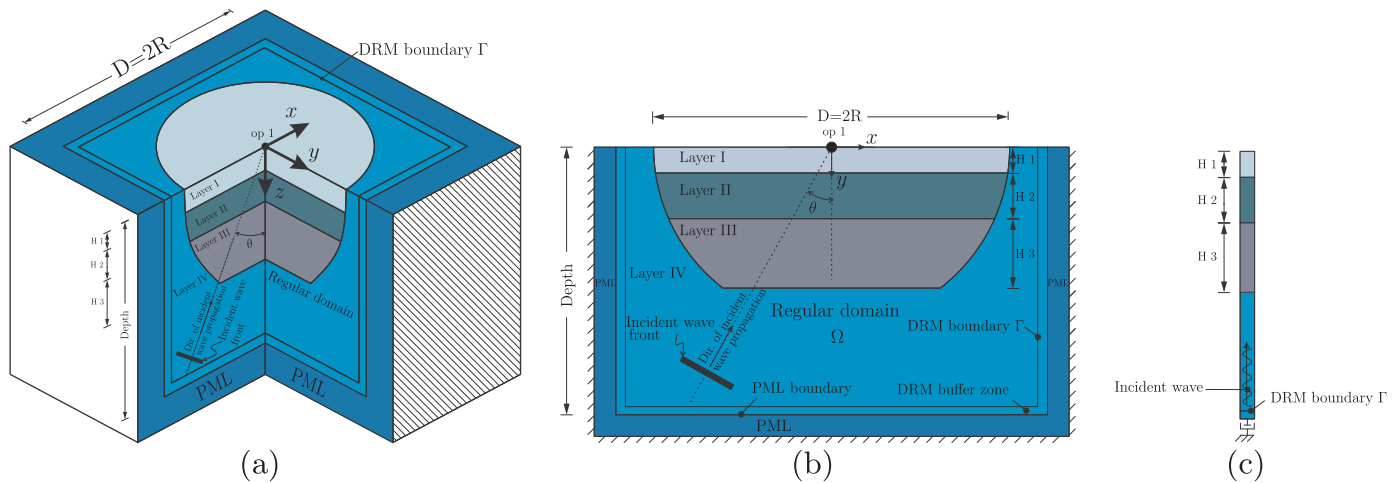
Fig. 20. Sedimentary valley models: (a) three-dimensional model, (b) two-dimensional model, and (c) equivalent one-dimensional model at observation point 1 (op1).

The difference between the maximum displacements on the surface is indicative of the valley edge effects. These results are in good agreement with the results reported in [25,27,28].

It is worth observing the surface amplification due to a vertically propagating SV wave in the two-dimensional model, as shown in Fig. 18(b): the maximum horizontal displacement is 4.31, occurs at the middle of the valley, while that of the P-wave is only 1.73, and the corresponding vertical displacements are 2.57 versus 3.54.

We plot the displacement contours due to a vertically propagating SV-wave at various instances in the two-dimensional model in Fig. 19. Notice that the particle motion for the SV incidence is normal to the direction of motion, thus, in the first snapshot, taken right after the plane wave enters the soft layer, the vertical displacement outside the soft soil vanishes. The wave velocity, and consequently the wavelength, is smaller in the soft layer. Therefore, to preserve the wave energy, the wave amplitude increases. Vertical displacements are generated within the domain, the moment the wave hits the soft soil. The maximum surface displacement occurs when the incident wave within the soft soil reflects back from the surface. The wave gets trapped within the soft soil and bounces back from the interface of the two materials and also from the surface. Even though the main incident front has left the domain in the last snapshot, there is still residual motion in the soft soil. The DRM boundary is also visible in the last snapshot, where there is a jump between the total motion in the regular domain and the scattered motion in the buffer between the DRM and the PML.

3.2.2. Example 2: A layered sedimentary valley: 1D vs. 2D vs. 3D

A number of densely populated areas, including Manhattan, NY, the San Fernando Valley, CA, or Seattle, WA [50,51], are situated on large, relatively low-velocity, basins, and are prone to strong earthquakes, due to their proximity to active seismic faults. There are several reports on the discrepancies between recorded motion and numerical computations due to complex site effects in heterogeneous geological configurations [15,52,53].

In this section, we attempt to numerically assess model dimensionality effects on the seismic response, using a typical multilayered, sediment-filled, valley. Toward this end, we compare the displacement time history on the surface using one-, two-, and three-dimensional models, for a vertically propagating P wave. We also compare the amplification due to SV-wave incidence between the two- and three-dimensional models.

Let us consider a typical sedimentary valley, similar to the Seattle basin, as shown in Fig. 20. The material properties and the depth of each layer have been summarized in Table 1. The semi-infinite domain is truncated to a $1700 \times 1700 \times 1200 \ \text{m}^3$, surrounded on its sides and

Table 1
Depths and material properties of the layered domain.

Layer	mass density ρ (kg/m³)	Poisson's ratio ν	shear velocity c_s (m/s)	compressional velocity c_p (m/s)	depth (H)
I	1800	0.25	200	346.41	30
II	2000	0.25	450	779.42	120
III	2200	0.25	600	1039.23	400
IV	2800	0.25	900	1558.85	550

bottom by a 120 m-thick PML. The medium is linear elastic with no material damping. The PML absorbing layer and the stiff half-space were discretized by quadratic elements with an element size of 20 m, resulting in six-element-thick PML. In the soft sediments, we use an element size of 15 m that allows for at least 20 points per dominant shear wavelength. The excitation is a plane incident wave (P or SV) in the form of a Ricker pulse with a central frequency of $f_r = 1.0 \text{Hz}$.

Fig. 21 shows the displacement time histories and their frequency content at observation point 1, located in the middle of the domain (Fig. 20). The maximum displacements are 3.50, 4.41, and 13.99, for the one-, two-, and three-dimensional models, respectively, i.e., the three-dimensional model yields a response 4 times greater than that of the one-dimensional model. Notice that if we look at the time history signal closely, we observe that the first pulse in all models is nearly identical in shape and magnitude, which in fact, represents the first reflection of the incident wave from the surface before the response gets polluted by the reflected waves from the layer interfaces. The maximum displacements for the one- and two-dimensional models both arise during the first pulse phase, and the rest of the response is characterized by smaller amplitudes. Interestingly, however, the maximum displacement in the three-dimensional model arises later in time as a result of the interference of Rayleigh waves generated from the edges of the sedimentary valley, with the reflected waves [15]. In summary, the main reason for having such a large difference between the maximum displacement obtained from the one-dimensional model and the two- or three-dimensional models is the inability of the one-dimensional model to capture mode conversions and Rayleigh waves. The total motion duration is over 25 s for the three-dimensional model, while the motion in the one- and two-dimensional models last only 3.5 and 10 s, respectively. Similar observations were reported in [25,27,28].

The frequency spectra of the three time histories in Fig. 21(b) show that all models amplify the frequencies between 0.7 to 1.5 Hz, though at different rates, while the three-dimensional model, exhibits another set of frequency amplifications between 1.5 to 2.1 Hz with higher
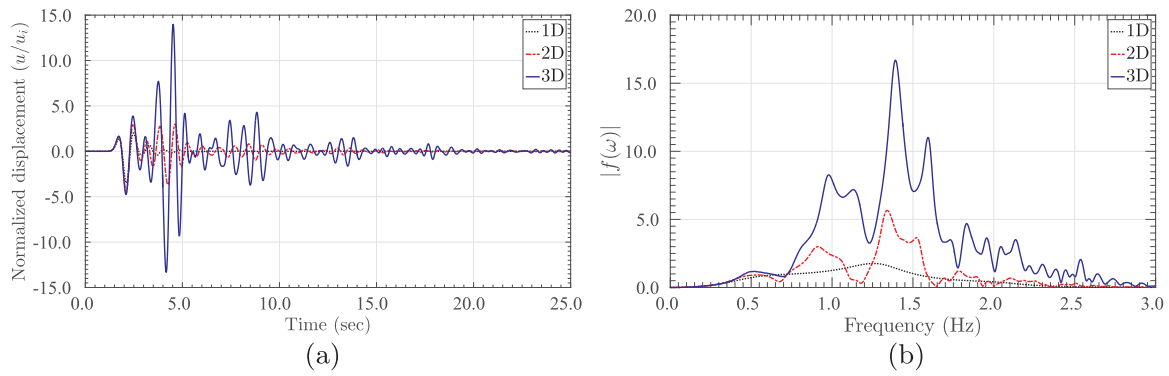
Fig. 21. (a) Displacement time histories and (b) their frequency spectra at observation point 1, for the one-, two-, and three-dimensional models due to the vertically propagating P-wave.
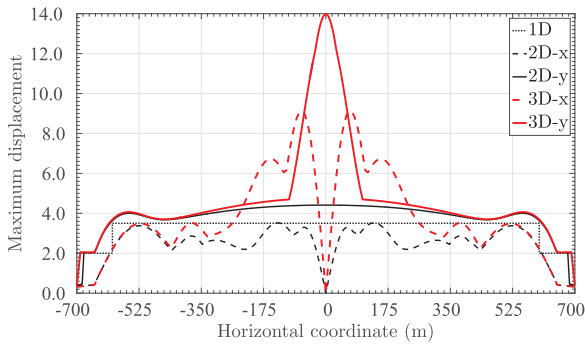

Fig. 22. The maximum displacement on the surface for all three models due to a vertically propagating P-wave.
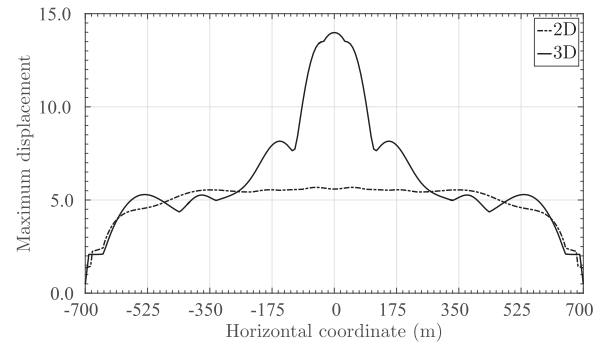

Fig. 24. The maximum surface displacement of the two- and three-dimensional models due to a vertically propagating SV-wave.

amplitudes than those exhibited at the lower frequencies. Recall that the central frequency of the incident wave is 1Hz, but, owing to the presence of the soft layers, amplification shifts to other frequencies.

Fig. 22 displays the maximum surface displacement for all three models. While a one-dimensional simulation predicts a constant amplification over the entire layered domain, the two- and three-dimensional models show spatially variable amplifications. Particularly, the constructive interaction of waves in the middle of the domain in the three-dimensional modal yields a large amplification, which cannot be seen even in the two-dimensional model. We remark again that the total duration of the incoming signal in this example is quite short, only 1.2 s, thus, the constructive interference of incoming and surface waves, which cannot be predicted by the one-dimensional model, may (very likely) lead to even larger amplifications if the input duration were to increase.

In a subsequent numerical experiment, we study the dimensionality

effects on the propagation of SV waves using the two- and three-dimensional models only. Fig. 23(a) displays the displacement time histories at observation point 1. The maximum displacements are 5.59 and 11.14, for the two- and three-dimensional models, respectively, i.e., the three-dimensional model yields a maximum displacement 2 times as large as that of the two-dimensional model. The total motion duration is over 30 s for the three-dimensional model, while the two-dimensional motion lasts no more than 15 s.

We would like to know whether the difference between the maximum displacements in the two- and three-dimensional models is localized (e.g., a small area in the middle of basin) or it can be also observed at other points on the surface as well. Toward this end, we plot (Fig. 24) the total maximum displacement on the surface of the two models in Fig. 24. The graph clearly shows that the interference of the waves along a large area in the middle of the three-dimensional domain results in remarkably strong amplification, which cannot be predicted
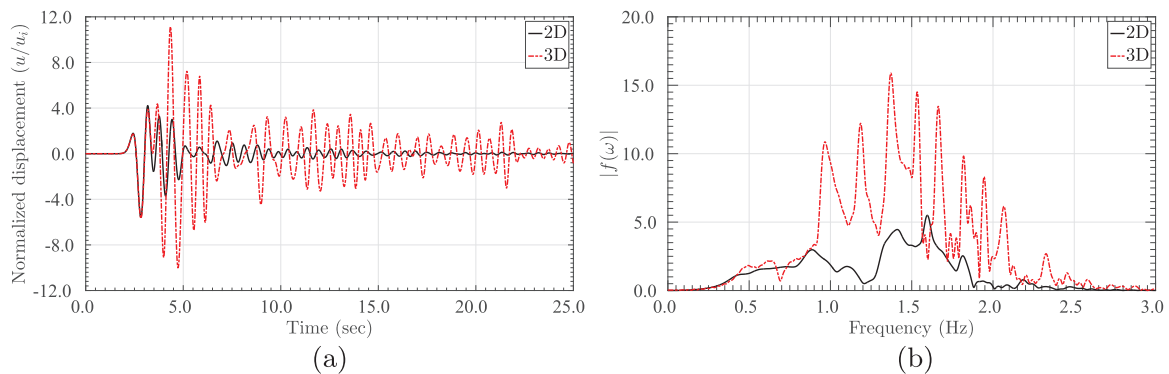

Fig. 23. Comparison of (a) displacement time histories and (b) their frequency spectra at observation point 1, for two- and three-dimensional domains due to vertically propagating SV wave.
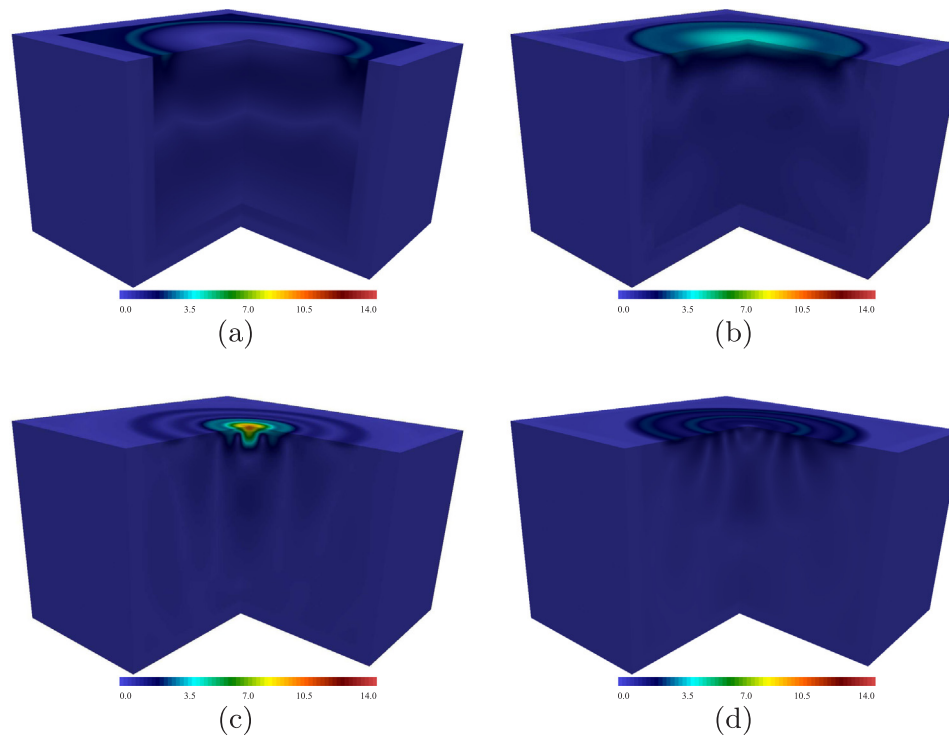
Fig. 25. Displacement contours at various instances due to a vertically propagating P-wave.

via a one- or even a two-dimensional model.

The displacement contours for the three-dimensional model are depicted in Fig. 25 at various instances. The first snapshot shows the moment where the waves enter the soft layer. The second snapshot shows the first reflection of the incident wave from the surface of the soft layers and the third one is at the moment when the maximum displacement occurs. The contours show how the amplification occurs within the layered domain due to energy being trapped within the soft layers.

4. Conclusions

The interest in understanding and quantifying seismic motion effects, particularly in regions with surface irregularities, such as hills, valleys, and alluvial basins, is strong, especially in light of the reported discrepancies between recorded surface strong motion data and numerical simulations. Even though the uncertainty in the velocity model remains a primary source of the discrepancies, the pervasive flat-surface assumption and the expediency-driven reduction of model dimensionality contribute decidedly to the discrepancies.

In this article, we reported model dimensionality effects on the seismic motion via time-domain numerical experiments in domains with irregular surfaces and in layered media. We concluded that one-dimensional models underestimate significantly the motion amplification, compared to two- and three-dimensional models, and reliance on such models should be avoided, particularly when site response analyses guide design decisions. Under certain conditions, two-dimensional

models may be adequate surrogates for three-dimensional models, but, in general, there is no good substitute to full-blown three-dimensional models, which should be encouraged especially when designing sensitive structures in seismic prone areas.

This study was limited to linear elastic isotropic material lossless behavior, exhibiting structured (non-arbitrary) heterogeneity. From a methodological point of view, the computational toolchain can readily accommodate arbitrarily heterogeneous geomorphology as well as various linear material attenuation models. Nonlinear behavior limited to a near-surface subdomain, can also be accommodated within the DRM framework, provided the domain exterior to the nonlinear subdomain remains linear. Consideration of anisotropy requires changes to the computational framework. From a physical point of view, the presence of nonlinearity and/or material damping will change, perhaps drastically, the response, but we expect that the general conclusion regarding the inadequacy of lower dimensionality models to remain valid.

Appendix A. Verification

We evaluate the validity of the formulation and numerical implementation by comparing the results against existing analytical and numerical solutions. Analytical solutions of wave propagation in a non-flat half-plane are scarce in the literature and are limited to only a few cases, mostly for SH-waves. Thus, to verify and assess the accuracy of our developed code, we resort to analytical solutions that are readily available for a flat homogeneous half-space. We first discuss closed-form solutions of wave motion in a flat homogeneous domain, and, then, we compare the three-dimensional numerical simulations with the exact solution.

A.1. Analytical solutions for a homogeneous half-space

The exact two-dimensional solution in the frequency-domain can be obtained by decomposing the displacement field, using the Helmholtz decomposition theorem, and substituting the results into Navier's equation [23,54]. Then, using d'Alembert's method, we can obtain the time-domain solution from the frequency-domain solution. If $\boldsymbol{u}$ is the displacement vector in a two-dimensional flat-surface half-space, then, the displacement field due to SV-wave incidence can be written as:

$$
\begin{bmatrix} u_x^s(x, y) \\ u_y^s(x, y) \end{bmatrix} = U_s^i \begin{bmatrix} +\cos\theta_s \\ +\sin\theta_s \end{bmatrix} f\left(-\frac{x}{c_s}\sin\theta_s + \frac{y}{c_s}\cos\theta_s + t \right)
$$
$$
+ U_s^r \begin{bmatrix} -\cos\theta_s \\ +\sin\theta_s \end{bmatrix} f\left(-\frac{x}{c_s}\sin\theta_s - \frac{y}{c_s}\cos\theta_s - t \right) + U_p^r \begin{bmatrix} +\sin\theta_p \\ +\cos\theta_p \end{bmatrix} f\left(-\frac{x}{c_p}\sin\theta_p - \frac{y}{c_p}\cos\theta_p + t \right),
$$
(A.1)

where u_x^s and u_y^s are the displacements within the domain in the x and y directions, respectively; θ_s is the angle of SV incidence, which is also equal to the angle of reflected SV-wave; θ_p is the angle of reflected P-wave derived according to Snell's law; c_s and c_p are shear and compressional wave velocities, respectively. $U_s^i = A_s^i k_s$ denotes the amplitude of the incoming SV-wave, and $U_s^r = A_s^r k_s$ and $U_p^r = A_p^r k_p$ are the amplitudes of the reflected SV- and P-waves, respectively. A_p^r and A_s^r are defined as:

$$
A_p^r = \frac{-2\,k^2\sin(2\theta_s)\cos(2\theta_s)}{\sin(2\theta_p)\sin(2\theta_s) + k^2\cos^2(2\theta_s)}A_s^i,
$$
(A.2a)

$$
A_s^r = \frac{\sin(2\theta_s)\sin(2\theta_p) - k^2\cos^2(2\theta_s)}{\sin(2\theta_p)\sin(2\theta_s) + k^2\cos^2(2\theta_s)}A_s^i,
$$
(A.2b)

where $k = c_p/c_s$.

In summary, while neglecting a few special cases, a plane SV-wave reflects from the flat surface of a homogeneous half-plane as P- and SV-waves as depicted in Fig. A.26(a). The first term of (A.1) denotes the equation for SV incident wave traveling at c_s velocity and an angle of incidence θ_s with an amplitude of $A_s^i k_s$; the second term indicates the reflected SV-wave traveling at the same velocity and angle with an amplitude of $A_s^r k_s$; and the third term is the reflected P-wave which has an amplitude of $A_p^r k_p$ and traveling in the domain at c_p velocity and angle of incidence θ_p.

Similarly, the displacement field due to P-wave incidence in a homogeneous flat half-plane can be expressed as:

$$
\begin{bmatrix} u_x^p(x, y) \\ u_y^p(x, y) \end{bmatrix} = U_p^i \begin{bmatrix} +\sin\theta_p \\ -\cos\theta_p \end{bmatrix} f\left(-\frac{x}{c_p}\sin\theta_p + \frac{y}{c_p}\cos\theta_p + t \right)
$$
$$
+ U_s^r \begin{bmatrix} +\cos\theta_s \\ -\sin\theta_s \end{bmatrix} f\left(-\frac{x}{c_s}\sin\theta_s - \frac{y}{c_s}\cos\theta_s - t \right) + U_p^r \begin{bmatrix} +\sin\theta_p \\ +\cos\theta_p \end{bmatrix} f\left(-\frac{x}{c_p}\sin\theta_p - \frac{y}{c_p}\cos\theta_p + t \right).
$$
(A.3)

u_x^p and u_y^p are the displacements within the domain in the x and y directions, respectively. $U_p^i = A_p^i k_p$ is the amplitude of the incoming P-wave, and $U_s^r = A_s^r k_s$ and $U_p^r = A_p^r k_p$ are the amplitudes of the reflected SV- and P-waves, respectively. A_p^r and A_s^r are computed as:

$$
A_p^r = \frac{\sin(2\theta_p)\sin(2\theta_s) - k^2\cos^2(2\theta_s)}{\sin(2\theta_p)\sin(2\theta_s) + k^2\cos^2(2\theta_s)}A_p^i,
$$
(A.4a)

$$
A_s^r = \frac{2\sin(2\theta_p)\cos(2\theta_p)}{\sin(2\theta_p)\sin(2\theta_s) + k^2\cos^2(2\theta_s)}A_p^i.
$$
(A.4b)

Fig. A.26(b) illustrates the typical reflection of a P-wave from a flat homogeneous half-space, excluding special cases. The first term of (A.3) denotes the equation for P incident wave traveling at the velocity of c_p and an angle of incidence θ_s with an amplitude of $A_p^i k_p$; the second term indicates the reflected SV-wave traveling at c_s and θ_s with an amplitude of $A_s^r K_s$; and the third term is the reflected P-wave which has an amplitude of $A_p^r k_p$ and traveling in the domain at the velocity c_p and angle of incidence θ_p.

In the above, the function $f = f(\tau)$ is any single-variable function that determines the shape of the wave. In this study, we use $f(\tau) = \sin(\tau)$ with a Ricker pulse signature, defined as:
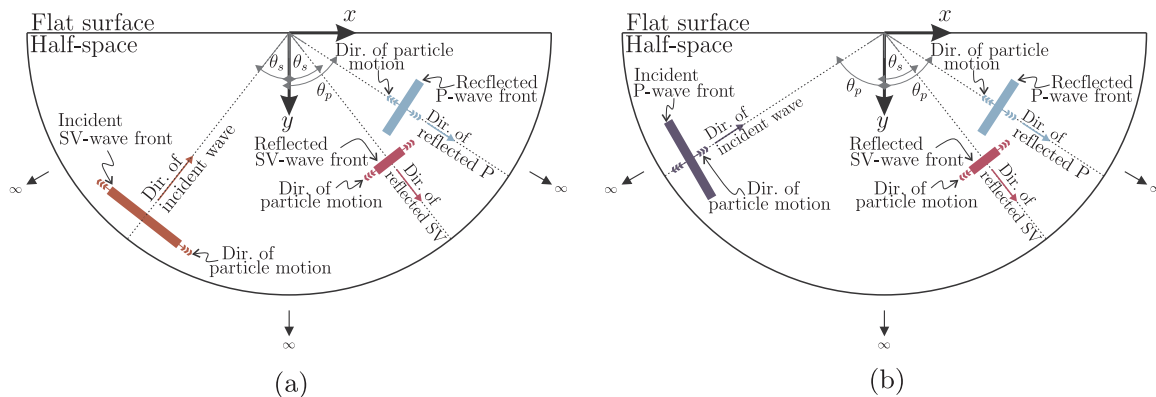

Fig. A.26. Schematic propagation of plane waves in a flat homogeneous half-space: (a) SV-wave, and (b) P-wave.
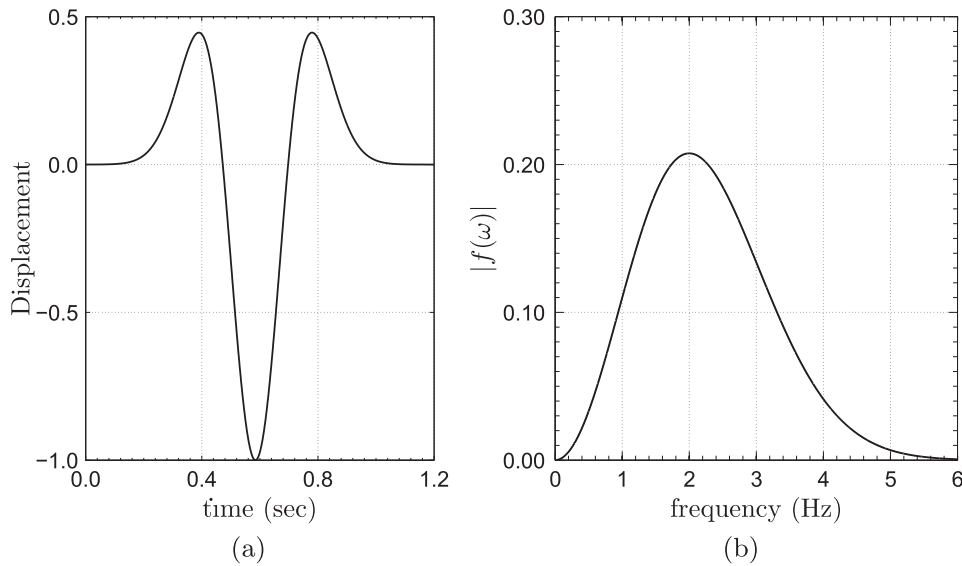
Fig. A.27. Ricker pulse (a) time history (b) its Fourier spectrum.

$$f(u; \tau) = \frac{(0.25u^2 - 0.5)e^{-0.25u^2} - 13e^{-13.5}}{0.5 + 13e^{-13.5}}, \quad \text{where} \quad u(\tau) = \omega_r \tau - 3\sqrt{6}, \quad 0 \leq t \leq \frac{6\sqrt{6}}{\omega_r},$$

(A.5)

where $\omega_r \ (= 2\pi f_r)$ denotes the characteristic central circular frequency of the pulse. For example, the displacement time-history, normalized with respect to the amplitude of the incident wave, and its corresponding Fourier spectrum are shown in Fig. A.27 for a frequency of $f_r = 2$Hz.

A.2. Verification of three-dimensional wave motion in a half-space

We compare the numerical simulation of wave motion in a three-dimensional, homogeneous, flat half-space with the analytical solutions obtained in A.1. The homogeneous half-space is truncated to a 800 m × 800 m × 300 m computational domain, surrounded on its sides and bottom by a 50 m-thick PML as shown in Fig. A.28. Quadratic hexahedral spectral elements (27-noded) of edge size 5 m are used to discretize the domain. The discretization results in a ten-element-thick PML with quadratic attenuation profile. The PML parameters α_0 and β_0 were set to 5.0 and 500m/s, respectively. The shear and compressional wave velocities are $c_s = 200$m/s and $c_p = 350$m/s, respectively, and no material damping mechanism is considered in the simulation. The frequency of the incident wave is 2Hz, and thus the shear wavelength is 100 m and the compressional wavelength is 175 m. The observation point to compare the analytical solution with the numerical results is located at (0 m, 150 m) (see Fig. A.28). Wave motion is implemented in the model using (A.1) and (A.3) with $f(\tau) = sin(\omega\tau)$ defined from 0 to π (half a cycle of a sinusoidal wave). τ is the wave phase and ω is the cyclic frequency of the wave.

A.2.1. Reflection of P-wave
The first verification example tests the reflection of a plane P incident wave of unit amplitude and the angle of incidence 15° from the flat surface
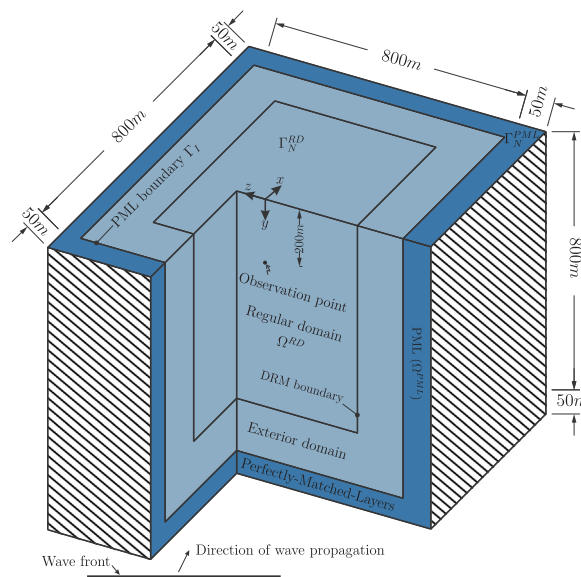

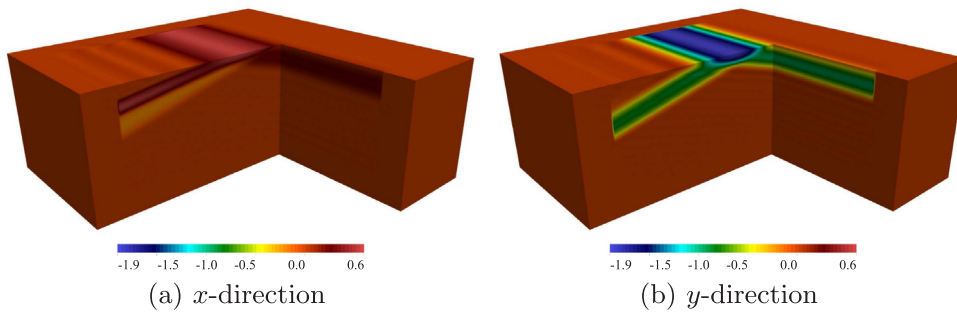**Fig. A.28.** Geometry of the half-space.

Fig. A.29. Propagation of P-wave in a flat half-space with an angle of incidence 15°.

(a) x-direction   (b) y-direction

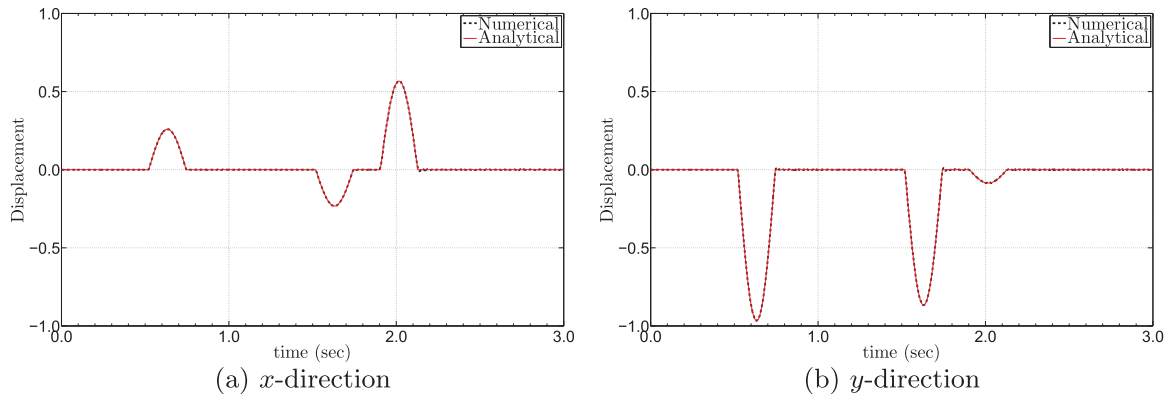(a) x-direction   (b) y-direction

Fig. A.30. Comparison of the time history of displacements at the observation point for the P incident wave.

of a half-space according to (A.3). Fig. A.29 depicts the snapshot of displacement field in the *x* and *y* directions (the displacement in the *z* direction in zero). As the wave hits the surface, it reflects back into the domain as P- and SV-waves. The reflected P-wave, which has the same angle as the incident wave, appears first due to the larger compressional velocity, with a reduction in the amplitude in comparison to the incident wave, owing to the redistribution of energy. Since the direction of motion has changed, both *x* and *y* displacements are negative. The SV-wave is following the P-wave with a shorter wavelength.

The time history of displacements in the *x* and *y* directions for the analytical and numerical solutions are displayed in Fig. A.30 for the observation point. A total agreement between the two time histories implies the accuracy of the developed formulation and the numerical simulation. Notice that three bumps are visible in the time history; the first bump is for the P incident wave, the second bump is for the reflected P-wave, and the third bump is due to the reflected SV-wave which is slower than the P-wave.

A.2.2. Reflection of SV-wave

The second three-dimensional verification example is the reflection of a plane SV incident wave of amplitude one and an angle of incidence of 15°, from the flat surface of a homogeneous domain. Fig. A.31 displays the displacement field in the *x* and *y* directions within the domain after the incident wave hits the flat surface. Three wave fronts can be seen in the displacement contour; the first one is the SV incidence, where the particle motion is normal to the direction of motion, thus, the *x* and *y* displacements are positive, the second one is the reflected P wave with positive displacements and greater angle of incidence and wavelength in comparison to the incidence, and the third one is the reflected SV wave with the same angle and wavelength as the incident wave.

The time history of displacement in the *x* and *y* directions for the propagation of SV-wave in the half-plane has been depicted in Fig. A.32 and is compared to the analytical solution. There is a good agreement between the two results.
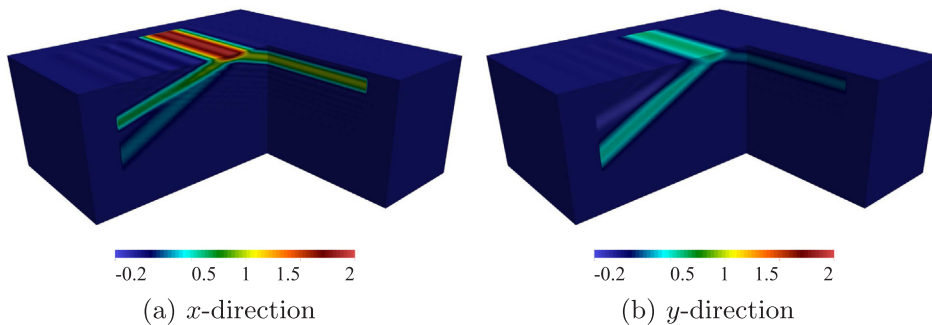
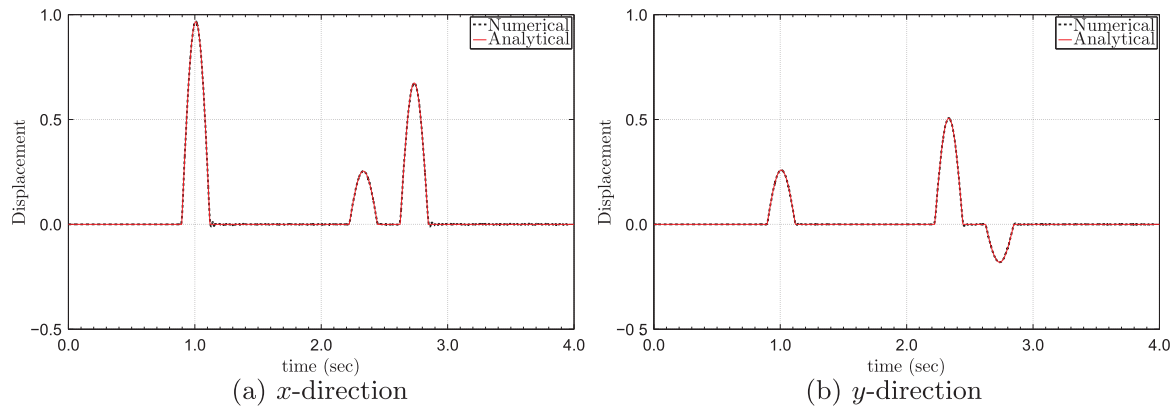**Fig. A.31.** Propagation of SV-wave in a flat half-plane with an angle of incidence 15°.

(a) x-direction   (b) y-direction

Fig. A.32. Comparison of the time history of displacements at the observation point for the P incident wave.

Appendix B. Remarks on adaptivity

Explicit solvers are highly scalable in parallel computing, but, in contrast to the implicit solvers, are conditionally stable, which means the solution diverges if the time-step exceeds an upper bound. Thus, the main challenge here is to determine the optimal time step which leads to a stable solution. Toward this end, most researchers use the Courant-Friedrichs-Lewy stability condition (CFL) to limit the time-step, which states that the distance traveled by the solution in one time-step, $c\Delta t$, must be less than the distance between two grid points. The following equations can be obtained for a structured domain [55]:

In 1D:
$$C = c_x \frac{\Delta t}{\Delta x}, \tag{B.1a}$$

In 2D:
$$C = \left(c_x \frac{\Delta t}{\Delta x}\right)^2 + \left(c_y \frac{\Delta t}{\Delta y}\right)^2, \tag{B.1b}$$

In 3D:
$$C = \left(c_x \frac{\Delta t}{\Delta x}\right)^2 + \left(c_y \frac{\Delta t}{\Delta y}\right)^2 + \left(c_z \frac{\Delta t}{\Delta z}\right)^2, \tag{B.1c}$$

where c_i is the largest wave velocity, Δx, Δy, and Δz are the minimum grid spacing in the x, y, and z directions, respectively. C is the Courant number, which should remain less than the maximum Courant number, C_{max}. The maximum Courant number is based on empirical experiments and is subject to change depending on the problem. The convention for a structured discretization is to assume $C_{max} = 1$, but this number reduces for an unstructured discretization. Therefore, in the absence of any firm relation for the time-step, a trial and error procedure is necessary to find the optimal time-step.

We demonstrate the efficiency of the explicit solvers in the following two-dimensional numerical experiments.

B.1. Example 1: Wave propagation in a homogeneous half-plane

Let us study the efficiency of the adaptive algorithm using the two-dimensional homogeneous model that we considered in Section A.2 for verification purposes. The maximum allowable time-step for this model with element of size $\Delta x = 2.5$m and the compressional wave velocity $c_p = 350$m/s is $\Delta t_{max} = 0.0025$s, as stated in (B.1) for $C_{max} = 1$. For a total time duration of $T = 4.5$s, the fourth-order Runge-Kutta with fixed time-step requires 1800 steps, which runs in 410 s on one CPU (average of ten simulations). However, running the same model, using the adaptive algorithm, requires only 1265 steps with a total runtime of 320s, i.e., 28% faster than the fixed time-step algorithm. Indeed, the computational cost of each step
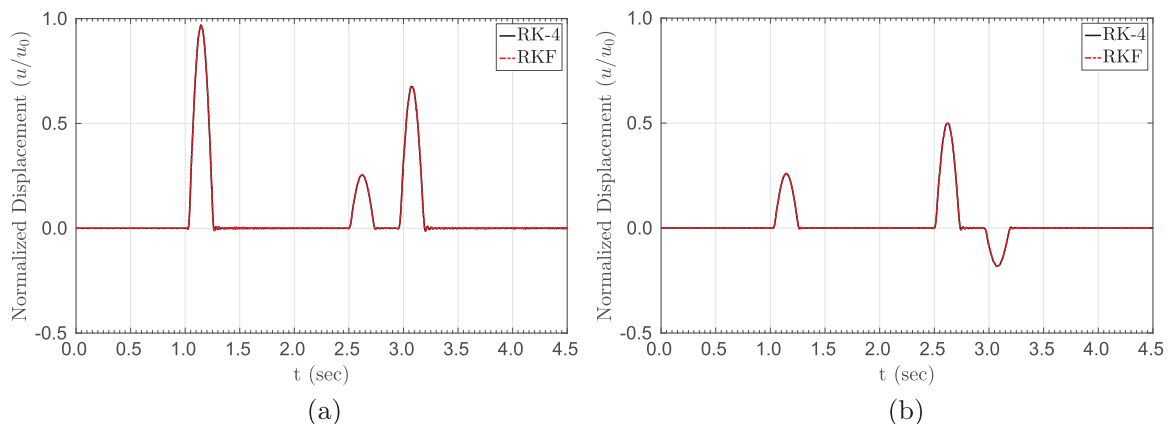

Fig. B.33. Comparison of the time histories of displacement computed from the fourth-order Runge-Kutta method and Runge-Kutta-Fehlberg with error tolerance $\varepsilon = 500$.
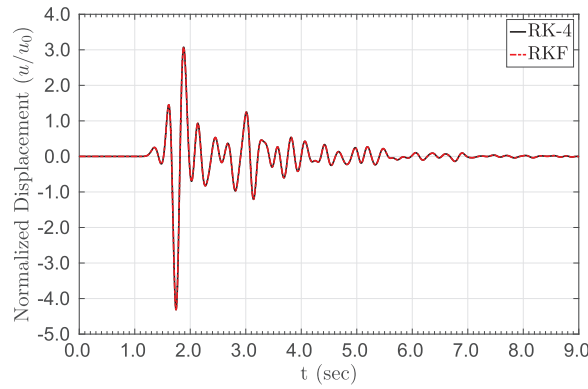
Fig. B.34. Comparison of the time histories of displacement computed from the fourth-order Runge-Kutta method and Runge-Kutta-Fehlberg.

of the adaptive algorithm is more than the fixed time-step algorithm, thus, the comparison of the total number of steps is not a firm measure of the efficiency of the adaptive algorithm, but the runtime. Fig. B.33 shows the time history of displacement at the observation point one for the fixed time-step algorithm and adaptive algorithm.

B.2. Example 2: Heterogeneous, sediment-filled valley

We use the heterogeneous, sediment-filled valley, described in Section 3.2.1, to verify the adaptive algorithm for an unstructured discretization. The valley shape and discretization is depicted in Fig. 15. Note that, in the absence of any criterion for choosing the time-step in an unstructured domain (the CFL condition is given only for structured discretization), we have no estimate of the time-step; thus, a trial and error process was inevitable. To have a rough estimate, one idea is that we find the minimum grid spacing and use the one-dimensional CFL limit. Using this approach the time-step should reduce to 59% of the one-dimensional CFL condition, i.e., from 0.00102s to 0.0006s. However, by using the adaptive algorithm, there is no need for any trial and error process. The displacement time histories at observation point 1 are depicted in Fig. B.34 for the fixed and adaptive time-step algorithms and show good agreement between the two methods.

In summary, we incorporated an adaptive algorithm that enhances the efficiency of the time integration scheme by computing the optimal time-step using the local truncation error at each time-step. This algorithm, in addition to being more efficient over the fixed time-step algorithm, eliminates concerns on how to choose the right time-step size (see [56] for details).

Appendix C. Submatrices in (2)

We use standard finite-dimensional subspaces $\Xi_h \subset \mathbf{H}^1(\Omega)$ and $\Upsilon_h \subset \mathscr{L}^2(\Omega)$, with basis functions $\mathbf{\Phi}$ and $\mathbf{\Psi}$, respectively. We then approximate $\mathbf{u}(\mathbf{x}, t)$ with $\mathbf{u}_h(\mathbf{x}, t) \in \Xi_h \times \mathsf{J}$, and $\mathbf{S}(\mathbf{x}, t)$ with $\mathbf{S}_h(\mathbf{x}, t) \in \Upsilon_h \times \mathsf{J}$, as detailed below:

$$\mathbf{u}_h\left(\mathbf{x}, t\right) = \begin{bmatrix} \mathbf{\Phi}^T(\mathbf{x})\mathbf{u}_x(t) \\ \mathbf{\Phi}^T(\mathbf{x})\mathbf{u}_y(t) \\ \mathbf{\Phi}^T(\mathbf{x})\mathbf{u}_z(t) \end{bmatrix},$$

(C.1a)

$$\mathbf{S}_h\left(\mathbf{x}, t\right) = \begin{bmatrix} \mathbf{\Psi}^T(\mathbf{x})\mathbf{S}_{xx}(t) & \mathbf{\Psi}^T(\mathbf{x})\mathbf{S}_{xy}(t) & \mathbf{\Psi}^T(\mathbf{x})\mathbf{S}_{xz}(t) \\ \mathbf{\Psi}^T(\mathbf{x})\mathbf{S}_{yx}(t) & \mathbf{\Psi}^T(\mathbf{x})\mathbf{S}_{yy}(t) & \mathbf{\Psi}^T(\mathbf{x})\mathbf{S}_{yz}(t) \\ \mathbf{\Psi}^T(\mathbf{x})\mathbf{S}_{zx}(t) & \mathbf{\Psi}^T(\mathbf{x})\mathbf{S}_{zy}(t) & \mathbf{\Psi}^T(\mathbf{x})\mathbf{S}_{zz}(t) \end{bmatrix}.$$

(C.1b)

λ and μ are the Lamé parameters and ρ is the density. Subscripts in the shape functions indicate derivatives.

$$\mathbf{K}_{\mathrm{RD}} = \int_{\Omega^{\mathrm{RD}}} \begin{bmatrix} \mathbf{K}_{xx} & \mathbf{K}_{xy} & \mathbf{K}_{xz} \\ \mathbf{K}_{yx} & \mathbf{K}_{yy} & \mathbf{K}_{yz} \\ \mathbf{K}_{zx} & \mathbf{K}_{zy} & \mathbf{K}_{zz} \end{bmatrix},$$

(C.2)

$$\mathbf{K}_{xx} = (\lambda + 2\mu)\mathbf{\Phi}_x\mathbf{\Phi}_x^T + \mu(\mathbf{\Phi}_y\mathbf{\Phi}_y^T + \mathbf{\Phi}_z\mathbf{\Phi}_z^T),$$

$$\mathbf{K}_{xy} = \lambda\mathbf{\Phi}_x\mathbf{\Phi}_y^T + \mu\mathbf{\Phi}_y\mathbf{\Phi}_x^T,$$

$$\mathbf{K}_{xz} = \lambda\mathbf{\Phi}_x\mathbf{\Phi}_z^T + \mu\mathbf{\Phi}_z\mathbf{\Phi}_x^T,$$

$$\mathbf{K}_{yx} = \lambda\mathbf{\Phi}_y\mathbf{\Phi}_x^T + \mu\mathbf{\Phi}_x\mathbf{\Phi}_y^T,$$

$$\mathbf{K}_{yy} = (\lambda + 2\mu)\mathbf{\Phi}_y\mathbf{\Phi}_y^T + \mu(\mathbf{\Phi}_x\mathbf{\Phi}_x^T + \mathbf{\Phi}_z\mathbf{\Phi}_z^T),$$

$$\mathbf{K}_{yz} = \lambda\mathbf{\Phi}_y\mathbf{\Phi}_z^T + \mu\mathbf{\Phi}_z\mathbf{\Phi}_y^T,$$

$$\mathbf{K}_{zx} = \lambda\mathbf{\Phi}_z\mathbf{\Phi}_x^T + \mu\mathbf{\Phi}_x\mathbf{\Phi}_z^T,$$

$$\mathbf{K}_{zy} = \lambda\mathbf{\Phi}_z\mathbf{\Phi}_y^T + \mu\mathbf{\Phi}_y\mathbf{\Phi}_z^T,$$

$$\mathbf{K}_{zz} = (\lambda + 2\mu)\mathbf{\Phi}_z\mathbf{\Phi}_z^T + \mu(\mathbf{\Phi}_x\mathbf{\Phi}_x^T + \mathbf{\Phi}_y\mathbf{\Phi}_y^T).$$

$$\mathbf{M}_{\mathrm{RD}} = \int_{\Omega^{\mathrm{RD}}} \rho\,\mathrm{diag}\!\left(\boldsymbol{\Phi\Phi}^T,\ \boldsymbol{\Phi\Phi}^T,\ \boldsymbol{\Phi\Phi}^T\right). \tag{C.3a}$$

$$\mathbf{M}_i^{\mathrm{PML}} = \int_{\Omega^{\mathrm{PML}}} i\,\rho\,\mathrm{diag}\!\left(\boldsymbol{\Phi\Phi}^T,\ \boldsymbol{\Phi\Phi}^T,\ \boldsymbol{\Phi\Phi}^T\right),\quad i=a,b,c,d. \tag{C.3b}$$

$$\mathbf{N}_i^{\mathrm{PML}} = \int_{\Omega^{\mathrm{PML}}} i\,\mathrm{diag}\!\left(\boldsymbol{\Psi\Psi}^T,\ \boldsymbol{\Psi\Psi}^T,\ \boldsymbol{\Psi\Psi}^T,\ 2\boldsymbol{\Psi\Psi}^T,\ 2\boldsymbol{\Psi\Psi}^T,\ 2\boldsymbol{\Psi\Psi}^T\right),\quad i=a,b,c,d. \tag{C.3c}$$

$$\mathbf{A}_{iu}^{\mathrm{PML}} = \int_{\Omega^{\mathrm{PML}}}
\begin{bmatrix}
\boldsymbol{\Phi}_x\boldsymbol{\Psi}^T\widehat{\lambda}^i_{yz} & & & \boldsymbol{\Phi}_y\boldsymbol{\Psi}^T\widehat{\lambda}^i_{xz} & \boldsymbol{\Phi}_z\boldsymbol{\Psi}^T\widehat{\lambda}^i_{xy} \\
& \boldsymbol{\Phi}_y\boldsymbol{\Psi}^T\widehat{\lambda}^i_{xz} & & \boldsymbol{\Phi}_x\boldsymbol{\Psi}^T\widehat{\lambda}^i_{yz} & & \boldsymbol{\Phi}_z\boldsymbol{\Psi}^T\widehat{\lambda}^i_{xy} \\
& & \boldsymbol{\Phi}_z\boldsymbol{\Psi}^T\widehat{\lambda}^i_{xy} & & \boldsymbol{\Phi}_x\boldsymbol{\Psi}^T\widehat{\lambda}^i_{yz} & \boldsymbol{\Phi}_y\boldsymbol{\Psi}^T\widehat{\lambda}^i_{xz}
\end{bmatrix}, \tag{C.4}$$

$$i=e,w,p,\quad \widehat{\lambda}^e_{jk}=\alpha_j\alpha_k,\quad \widehat{\lambda}^p_{jk}=\alpha_j\beta_k+\beta_j\alpha_k,\quad \widehat{\lambda}^w_{jk}=\beta_j\beta_k,\quad j,k=x,y,z.$$

$$\mathbf{A}_{il}^{\mathrm{PML}} = \int_{\Omega^{\mathrm{PML}}}
\begin{bmatrix}
\mathbf{A}_{x1}^{\mathrm{PML}} & \mathbf{A}_{x2}^{\mathrm{PML}} & \mathbf{A}_{x3}^{\mathrm{PML}} & \mathbf{A}_{x4}^{\mathrm{PML}} & \mathbf{A}_{x5}^{\mathrm{PML}} \\
\mathbf{A}_{y1}^{\mathrm{PML}} & \mathbf{A}_{y2}^{\mathrm{PML}} & \mathbf{A}_{y3}^{\mathrm{PML}} & \mathbf{A}_{y4}^{\mathrm{PML}} & & \mathbf{A}_{y6}^{\mathrm{PML}} \\
\mathbf{A}_{z1}^{\mathrm{PML}} & \mathbf{A}_{z2}^{\mathrm{PML}} & \mathbf{A}_{z3}^{\mathrm{PML}} & & \mathbf{A}_{z5}^{\mathrm{PML}} & \mathbf{A}_{z6}^{\mathrm{PML}}
\end{bmatrix}, \tag{C.5}$$

$$\mathbf{A}_{x1}^{\mathrm{PML}}=(\lambda+2\mu)\boldsymbol{\Phi}_x\boldsymbol{\Psi}^T\widehat{\lambda}^i_{yz},\qquad \mathbf{A}_{y1}^{\mathrm{PML}}=\lambda\boldsymbol{\Phi}_y\boldsymbol{\Psi}^T\widehat{\lambda}^i_{xz},\qquad \mathbf{A}_{z1}^{\mathrm{PML}}=\lambda\boldsymbol{\Phi}_z\boldsymbol{\Psi}^T\widehat{\lambda}^i_{xy},$$

$$\mathbf{A}_{x2}^{\mathrm{PML}}=\lambda\boldsymbol{\Phi}_x\boldsymbol{\Psi}^T\widehat{\lambda}^i_{yz},\qquad \mathbf{A}_{y2}^{\mathrm{PML}}=(\lambda+2\mu)\boldsymbol{\Phi}_y\boldsymbol{\Psi}^T\widehat{\lambda}^i_{xz},\qquad \mathbf{A}_{z2}^{\mathrm{PML}}=\lambda\boldsymbol{\Phi}_z\boldsymbol{\Psi}^T\widehat{\lambda}^i_{xy},$$

$$\mathbf{A}_{x3}^{\mathrm{PML}}=\lambda\boldsymbol{\Phi}_x\boldsymbol{\Psi}^T\widehat{\lambda}^i_{yz},\qquad \mathbf{A}_{y3}^{\mathrm{PML}}=\lambda\boldsymbol{\Phi}_y\boldsymbol{\Psi}^T\widehat{\lambda}^i_{xz},\qquad \mathbf{A}_{z3}^{\mathrm{PML}}=(\lambda+2\mu)\boldsymbol{\Phi}_z\boldsymbol{\Psi}^T\widehat{\lambda}^i_{xy},$$

$$\mathbf{A}_{x4}^{\mathrm{PML}}=2\mu\boldsymbol{\Phi}_y\boldsymbol{\Psi}^T\widehat{\lambda}^i_{xz},\qquad \mathbf{A}_{y4}^{\mathrm{PML}}=2\mu\boldsymbol{\Phi}_x\boldsymbol{\Psi}^T\widehat{\lambda}^i_{yz},\qquad \mathbf{A}_{z5}^{\mathrm{PML}}=2\mu\boldsymbol{\Phi}_x\boldsymbol{\Psi}^T\widehat{\lambda}^i_{yz},$$

$$\mathbf{A}_{x5}^{\mathrm{PML}}=2\mu\boldsymbol{\Phi}_z\boldsymbol{\Psi}^T\widehat{\lambda}^i_{xy},\qquad \mathbf{A}_{y6}^{\mathrm{PML}}=2\mu\boldsymbol{\Phi}_z\boldsymbol{\Psi}^T\widehat{\lambda}^i_{xy},\qquad \mathbf{A}_{z6}^{\mathrm{PML}}=2\mu\boldsymbol{\Phi}_y\boldsymbol{\Psi}^T\widehat{\lambda}^i_{xz},$$

$$\widehat{\lambda}^e_{jk}=\alpha_j\alpha_k,\qquad \widehat{\lambda}^p_{jk}=\alpha_j\beta_k+\beta_j\alpha_k,\qquad \widehat{\lambda}^w_{jk}=\beta_j\beta_k,$$

$$i=e,w,p,\qquad j,k=x,y,z.$$

$$\mathbf{f}_{\mathrm{RD}} = \int_{\Gamma_N^{\mathrm{RD}}}
\begin{bmatrix}
\boldsymbol{\Phi}\,g_x(\mathbf{x},t) \\
\boldsymbol{\Phi}\,g_y(\mathbf{x},t) \\
\boldsymbol{\Phi}\,g_z(\mathbf{x},t)
\end{bmatrix}
+ \int_{\Omega^{\mathrm{RD}}}
\begin{bmatrix}
\boldsymbol{\Phi}\,b_x(\mathbf{x},t) \\
\boldsymbol{\Phi}\,b_y(\mathbf{x},t) \\
\boldsymbol{\Phi}\,b_z(\mathbf{x},t)
\end{bmatrix}. \tag{C.6}$$

References

[1] Pratt TL, Brocher TM, Weaver CS, Creager KC, Snelson CM, Crosson RS, et al. Amplification of seismic waves by the Seattle Basin, Washington State. Bull Seismol Soc Am 2003;93(2):533–45.

[2] Çelebi M. Topographical and geological amplifications determined from strong-motion and aftershock records of the 3 march 1985 chile earthquake. Bull Seismol Soc Am 1987;77(4):1147–67.

[3] Çelebi M. Topographical and geological amplification: case studies and engineering implications. Struct Saf 1991;10:199–217.

[4] Hartzell SH, Carver DL, King KW. Initial investigation of site and topographic effects at Robinwood Ridge, California. Bull Seismol Soc Am 1994;84(5):1336–49.

[5] Bouchon M, Barker JS. Seismic response of a hill: the example of Tarzana, California. Bull Seismol Soc Am 1996;86(1A):66–72.

[6] Assimaki D, Gazetas G, Kausel E. Effects of local soil conditions on the topographic aggravation of seismic motion: parametric investigation and recorded field evidence from the 1999 Athens earthquake. Bull Seismol Soc Am 2005;95(3):1059–89.

[7] Assimaki D, Kausel E, Gazetas G. Wave propagation and soil-structure interaction on a cliff crest during the 1999 Athens Earthquake. Soil Dyn Earthq Eng 2005;25(7–10):513–27.

[8] Graizer V. Low-velocity zone and topography as a source of site amplification effect on Tarzana hill, California. Soil Dyn Earthq Eng 2009;29(2):324–32.

[9] Imperatori W, Mai PM. The role of topography and lateral velocity heterogeneities on near-source scattering and ground-motion variability. Geophys J Int 2015;202(3):2163–81.

[10] Massa M, Lovati S, D'Alema E, Ferretti G, Bakavoli M. An experimental approach for estimating seismic amplification effects at the top of a ridge, and the implication for ground-motion predictions: the case of Narni, Central Italy. Bull Seismol Soc Am 2010;100(6):3020–34.

[11] Buech F, Davies TR, Pettinga JR. The Little Red Hill Seismic Experimental Study: topographic effects on ground motion at a bedrock-dominated mountain edifice. Bull Seismol Soc Am 2010;100(5A):2219–29.

[12] Geli L, Bard PY, Jullien B. The effect of topography on earthquake ground motion: a review and new results. Bull Seismol Soc Am 1988;78(1):42–63.

[13] Bard PY. Microtremor measurements: A tool for site effect estimation? In: Irikura, Kudo, Okada, and Sasatani, editors, The effects of surface geology on seismic motion; 1999, volume 3, p. 1251–79.

[14] Semblat JF, Kham M, Parara E, Bard PY, Pitilakis K, Makra K, et al. Seismic wave amplification: basin geometry vs soil layering. Soil Dyn Earthq Eng 2005;25(7–10):529–38.

[15] Field EH. Spectral amplification in a sediment-filled valley exhibiting clear basin-edge-induced waves. Bull Seismol Soc Am 1996;86(4):991–1005.

[16] Sánchez-Sesma FJ. Diffraction of elastic waves by three-dimensional surface irregularities. Bull Seismol Soc Am 1983;73(6A):1621–36.

[17] Dravinski M, Mossessian TK, Eshraghi H, Kagami H. Predominant motion of the Los Angeles sedimentary basin. Eng Anal Bound Elem 1991;8(4):206–14.

[18] Sánchez-Sesma FJ, Luzón F. Seismic response of three-dimensional alluvial valleys for incident P, S, and Rayleigh waves. Bull Seismol Soc Am 1995;85(1):269–84.

[19] Vai R, Castillo-Covarrubias JM, Sánchez-Sesma FJ, Komatitsch D, Vilotte J-P. Elastic wave propagation in an irregularly layered medium. Soil Dyn Earthq Eng 1999;18(1):11–8.

[20] Bouckovalas GD, Papadimitriou AG. Numerical evaluation of slope topography effects on seismic ground motion. Soil Dyn Earthq Eng 2005;25(7–10):547–58.

[21] Makra K, Chávez-García FJ, Raptakis D, Pitilakis K. Parametric analysis of the seismic response of a 2D sedimentary valley: implications for code implementations of complex site effects. Soil Dyn Earthq Eng 2005;25(4):303–15.

[22] Meza-Fajardo KC, Semblat JF, Chaillat S, Lenti L. Seismic wave amplification in 3d alluvial basins: 3d/1d amplification ratios from fast multipole bem simulations. Bull Seismol Soc Am 2016;106(3):1267.

[23] Poursartip B, Fathi A, Kallivokas LF. Seismic wave amplification by topographic features: a parametric study. Soil Dyn Earthq Eng 2017;92:503–27.

[24] Wood CM, Cox BR. Experimental data set of mining-induced seismicity for studies of full-scale topographic effects. Earthq Spectra 2015;31(1):541–64.

[25] Makra K, Chávez-García FJ. Site effects in 3D basins using 1D and 2D models: an evaluation of the differences based on simulations of the seismic response of Euroseistest. Bull Earthq Eng 2016;14(4):1177–94. (April).

[26] Riepl J, Zahradník J, Plicka V, Bard P-Y. About the efficiency of numerical 1-D and 2-D modelling of site effects in basin structures. Pure Appl Geophys 2000;157(3):319–42. (March).

[27] Hisada Y, Yamamoto S. One-, two- and three dimensional site effects in sediment filled basins. In: Proceedings of the 11th world conference on earthquake

engineering; 1996.

[28] Bielak J, Hisada Y, Bao H, Xu J. One- vs two- or three-dimensional effects in sedimentary valleys. In: Proceedings of the 12th world conference on earthquake engineering; 2000.

[29] Smerzini C, Paolucci Roberto, Stupazzini Marco. Comparison of 3D, 2D and 1D numerical approaches to predict long period earthquake ground motion in the Gubbio plain, Central Italy. Bull Earthq Eng 2011;9(6):2007–29. (December).

[30] Madiai C, Facciorusso J, Gargini E, Baglione M. 1D Versus 2D Site Effects from Numerical Analyses on a Cross Section at Barberino Di Mugello (Tuscany, Italy). Procedia Engineering, 158:499 - 504, 2016. VI Italian Conference of Researchers in Geotechnical Engineering, CNRIG2016 - Geotechnical Engineering in Multidisciplinary Research: from Microscale to Regional Scale, 22–23 September 2016, Bologna (Italy).

[31] Semblat JF. Modeling seismic wave propagation and amplification in 1d/2d/3d linear and nonlinear unbounded media. Int J Geomech 2011;11(6):440–8.

[32] Komatitsch D, Tromp J. Introduction to the spectral element method for three-dimensional seismic wave propagation. Geophys J Int 1999;139(3):806–22.

[33] Komatitsch D, Vilotte J-P. The spectral element method: an efficient tool to simulate the seismic response of 2D and 3D geological structures. Bull Seismol Soc Am 1998;88(2):368–92.

[34] Peter D, Komatitsch D, Luo Y, Martin R, Le Goff N, Casarotti E, et al. Forward and adjoint simulations of seismic wave propagation on fully unstructured hexahedral meshes. Geophys J Int 2011;186(2):721–39.

[35] Poursartip B, Kallivokas LF. An Integrated Approach for the Large-Scale Simulationof Sedimentary Basins to Study Seismic Wave Amplification. In: AGU Fall Meeting Abstracts, Decemeber 2015.

[36] Fathi A, Poursartip B, Kallivokas LF. Time-domain hybrid formulations for wave simulations in three-dimensional PML-truncated heterogeneous media. Int J Numer Methods Eng 2015;101(3):165–98.

[37] Kallivokas LF, Bielak J, MacCamy RC. Symmetric local absorbing boundaries in time and space. J Eng Mech 1991;117:2027–48.

[38] Bielak J, Kallivokas LF, Xu J, Monopoli R. Finite element absorbing boundary for the wave equation in a half-place with an application to engineering seismology. In: Proceedings of the third international conference on mathematical and numerical aspects of wave propagation, INRIA-SIAM; 1995. p. 489–98.

[39] Givoli D, Neta B. High-order non-reflecting boundary scheme for time-dependent waves. J Comput Phys 2003;186(1):24–46.

[40] Hagstrom T, Warburton T. A new auxiliary variable formulation of high-order local radiation boundary conditions: corner compatibility conditions and extensions to first-order systems. Wave Motion 2004;39(4):327–38.

[41] Kucukcoban S, Kallivokas LF. Mixed perfectly-matched-layers for direct transient analysis in 2D elastic heterogeneous media. Comput Methods Appl Mech Eng 2011;200(1–4):57–76.

[42] Bielak J, Christiano P. On the effective seismic input for non-linear soil-structure interaction systems. Earthq Eng Struct Dyn 1984;12(1):107–19.

[43] Bielak J, Loukakis K, Hisada Y, Yoshimura C. Domain reduction method for three-dimensional earthquake modeling in localized regions, Part I: Theory. Bull Seismol Soc Am 2003;93(2):817–24.

[44] Cremonini MG, Christiano P, Bielak J. Implementation of effective seismic input for soil-structure interaction systems. Earthq Eng Struct Dyn 1988;16(4):615–25.

[45] Yoshimura C, Bielak J, Hisada Y, Fernández A. Domain reduction method for three-dimensional earthquake modeling in localized regions, Part II: verification and applications. Bull Seismol Soc Am 2003;93(2):825–41.

[46] Komatitsch D, Tsuboi S, Tromp J. The spectral-element method in seismology. American Geophysical Union; 2005. p. 205–27.

[47] Casarotti E, Stupazzini M, Lee S, Komatitsch D, Piersanti A, Tromp J. Cubit and seismic wave propagation based upon the spectral-element method: An advanced unstructured mesher for complex 3D geological media. In: M.L. Brewer and D. Marcum, editors, Proceedings of the 16th international meshing roundtable, Springer, Berlin Heidelberg; 2008. p. 579–97.

[48] Quarteroni A, Sacco R, Saleri F. Numerical mathematics. Texts in applied mathematics. Springer; 2010.

[49] King JL, Tucker BE. Observed variations of earthquake motion across a sediment-filled valley. Bull Seismol Soc Am 1984;74(1):137–51.

[50] Frankel A, Stephenson W. Three-dimensional simulations of ground motions in the Seattle region for earthquakes in the Seattle Fault Zone. Bull Seismol Soc Am 2000;90(5):1251–67.

[51] Snelson CM, Brocher TM, Miller KC, Pratt TL, Tréhu AM. Seismic amplification within the Seattle Basin, Washington State: insights from SHIPS seismic tomography experiments. Bull Seismol Soc Am 2007;97(5):1432–48.

[52] Bard PY, Bouchon M. The two-dimensional resonance of sediment-filled valleys. Bull Seismol Soc Am 1985;75(2):519–41.

[53] Havenith HB, Fäh D, Alvarez-Rubio S, Roten D. Response spectra for the deep sediment-filled Rhône valley in the Swiss Alps. Soil Dyn Earthq Eng 2009;29(1):17–38.

[54] Graff KF. Wave motion in elastic solids. Dover books on engineering series. Dover Publications; 1975.

[55] Strang G. Computational science and engineering. New york, NY: Wellesley-Cambridge Press; 2007.

[56] Poursartip B. Topographic amplification of seismic motion (Ph.D. thesis). Texas, USA: The University of Texas at Austin; 2017. May.